2004

Innovative cooling configurations for low emission gas turbine combustors

Ryan Thomas Hebert
Louisiana State University and Agricultural and Mechanical College, rheber7@lsu.edu

INNOVATIVE COOLING CONFIGURATIONS FOR LOW EMISSION GAS TURBINE COMBUSTORS

A Thesis

Submitted to the Graduate Faculty of the
Louisiana State University and
Agricultural and Mechanical College
in partial fulfillment of the
requirements for the degree of
Master of Science in Mechanical Engineering

in

The Department of Mechanical Engineering

by
Ryan Thomas Hebert
B.S., Louisiana State University, 2002
August 2004

ACKNOWLEDGEMENTS

The successes I have achieved throughout my educational journey would certainly not have been possible without the unending support of my mentor, my family, and my friends. I especially want to thank my adoring wife Jennifer for putting up with all late nights and long weekends I spent at the lab. Without her love and support all the accomplishments in the world would mean nothing. I would also like to thank Dr. Ekkad for his guidance, wisdom, and most importantly his friendship. It seems like yesterday I was simply trying to get a flag raised so I could schedule classes, when unbeknownst to me, I was caught up in the world wind that is Dr. Ekkad. His influence was undoubtedly the driving force behind all of the educational and professional achievements I have had since that seemingly random morning three years ago. I could not imagine a better mentor. I also must thank of my lab mates, both past and present. Special thanks go out to Hasan Nasir and Eric Esposito for their assistance in a multitude of tasks I could not have performed without their help. My thanks also go out to my classmates Jonathon Lagrone and Ross Gustafson. Having such great guys to collaborate with made my graduate studies infinitely more enjoyable. Last and certainly not least I have to thank my family. The unconditional support and encouragement I received from my parents was a crucial part of my educational journey. Any time I began to falter, they were there to reassure me and give me the confidence I needed to continue. Their love and devotion is unmatched and I am truly lucky to have such wonderful parents. I would also like to thank the Halls for believing in me and entrusting me with the well-being of their baby. I will never let them down. Finally, I would like to thank my sister, Kate, and my brothers, Ben and Will. Now that this part of my journey is almost complete and I reflect on my past experiences, I know that with such an amazing family I can overcome anything life throws my way and all my future will be as least as enjoyable as this one has been.

TABLE OF CONTENTS

LIST OF TABLES

LIST OF FIGURES

NOMENCLATURE

D_h	inlet channel hydraulic diameter
e	rib height
h	local convection heat transfer coefficient
H	distance between the jet plate and target plate
k	thermal conductivity
α	thermal diffusivity
L	length of target plate
Nu_D	Nusselt number
P	rib pitch
Re_D	Reynolds number
S	jet-to-jet spacing
t	time of liquid crystal color change
T_i	initial temperature of test section
T_w	green color change temperature of the liquid crystals
T_m	mainstream temperature of the flow
U	average jet velocity
X	streamwise location on target plate
Y	spanwise location on target plate
ν	fluid kinematic viscosity
τ	time step for Duhamel's superposition
N	number of edge nodes
$q_{\Delta t}$	heat flux at the Δt time step
q_f	heat flux for the fine mesh
q_m	heat flux for the medium mesh

q_c heat flux for the coarse mesh

$e_{\Delta t}$ time step error

e_d discretization error

e_T total error

ABSTRACT

Presently, effective cooling of modern low NOx combustor liners is achieved through combinations of innovative impingement configurations and other heat transfer enhancement methods. An inherent characteristic of conventional impingement configurations is the occurrence of downstream heat transfer degradation due to increased crossflow effects. In the present study, two different impingement configurations are studied. Both impingement configurations examined in this study aim to increase heat transfer effectiveness by reducing the detrimental effects of spent air crossflow. In Part I, a combination technique wherein impingement is combined with ribs placed in between impingement rows is studied. Three configurations with increased rib placements and reduced impingement holes are studied. Each case is compared to a pure impingement configuration for the same jet Reynolds number. In Part II, an innovative impingement configuration, called the zero-crossflow design, is examined. In this design, spent air is directed away from the target surface in an attempt to completely eliminate the detrimental effects of crossflow by reducing its interaction with impingement jets. Three different jet arrays with decreasing numbers of impingement jets are examined in this part of the study. For all test cases, three jet Reynolds numbers (10000, 20000, and 30000) are studied.

Detailed heat transfer distributions are obtained through out the study using a transient liquid crystal technique. Results from Part I show that the presence of ribs increases jet impingement heat transfer along the entire target surface. The crossflow improvements of this combination provide higher heat transfer with reduced cooling air requirements, even though some crossflow degradation is still present. In contrast, the zero-crossflow design of Part II shows minimal heat transfer degradation due to crossflow. This design also displays the ability to produce symmetric heat transfer distributions, which are almost completely independent of the exit flow direction. Finally, the sparse arrays of both parts of the study show more efficient cooling by achieving similar levels of heat transfer with greatly reduced coolant flows.

C H A P T E R 1

INTRODUCTION

Turbine Engine designers have consistently pushed the envelope of existing technologies to improve the performance and efficiency of the gas turbine engine. In the early stages of jet engine development, most innovations were driven by the military impetus of World War II, with maximum engine performance being the main objective. However, the creation of two new gas turbine applications altered the focus of engine designers across the globe. The first occurred in the 1960's with the explosion of commercial air travel. For the first time, the performance envelope of many gas turbines was focused on relatively slow, efficient flights of large capacity aircraft. Additionally, the power generation industry began a widespread implementation of industrial turbines in power plants around the world. These two industries created an entirely new incentive to push engineers to design much larger and more efficient turbines.

Engineers realized that increases in pressure ratio and turbine inlet temperature could lead to improved efficiency, increased thrust, and lower fuel consumption. Unfortunately, each of these increases had a detrimental effect on engine durability, especially in the combustor and turbine regions. Higher efficiencies and fuel burn temperatures led to increased radiative heating of the combustor's inner liner, and raising turbine inlet temperatures hindered the use of convective cooling on this component[1].

1.1 Cooling in Gas Turbine Combustors

Many advances in cooling and material technologies eventually led to the development of more sophisticated engines that could operate much closer to the material melting point while sustaining manageable amounts of wear and fatigue. Presently, engine designers employ complex

cooling schemes, such as impingement, film cooling, and trip strips, to increase engine durability and achieve performance criteria. In each of these cooling methods, relatively cooler air from the compressor stages is routed around the combustor and injected into different cooling passages throughout the engine. These passages then use a multitude of heat transfer enhancement techniques to remove heat from various engine components. Finally, the coolant rejoins the mainstream air in the turbine stage through discrete holes on the surface of the turbine blades creating a protective film cooling layer.

One of the harshest environments in a gas turbine engine is the combustor. Extremely high temperatures and tremendous thermal gradients exist on this component, and special measures must be taken to ensure its durability. To achieve adequate performance over the 30,000-hour operating life of modern lean premixed low emission combustors these extreme thermal loads must be controlled. For example, some nickel- or cobalt- combustor alloys, like Nimonic 75, Hastelloy x, and HS 188, cannot exceed operating temperatures of 1100 K. After this point, significant degradation of structural integrity occurs[1].

Initially, all combustor cooling methods utilized film cooling mechanisms to reduce the temperature of inner liner of the combustion chamber. However, as pressure ratios and engine temperatures continued to rise, as much as one-third of the total combustor airflow had to be used to film cool the liner[1]. This design also created richer burning in the combustor core and caused a centerline peak in temperature. Some of the rich fuel did not completely combust. This resulted in increased emission of pollutants such as NOx, CO, and unburnt hydrocarbons. Figure 1 shows one such film cooling configuration.

Over the past 20 years, both federal and state governments have placed serious regulations on the emission of these pollutants. To achieve a significant reduction in emissions, one of the main methods designers have focused on is lean pre-mixed combustors, which are combustors with a low fuel to air ratio. *Lean combustion* increases the mixing of fuel and air by adding more air to the mainstream combustor flow and reducing the amount of cool air injected through the liner. This type of combustion increases the degree of complete fuel combustion and reduces the flame

temperature. Lean combustion requirements have caused a severe reduction in the allowable coolant and have all but eliminated the use of film cooling in combustor liners. With the exclusion of film cooling, engine designers have to employ other heat transfer enhancement techniques to cool the lean pre-mixed combustor liners from the backside.

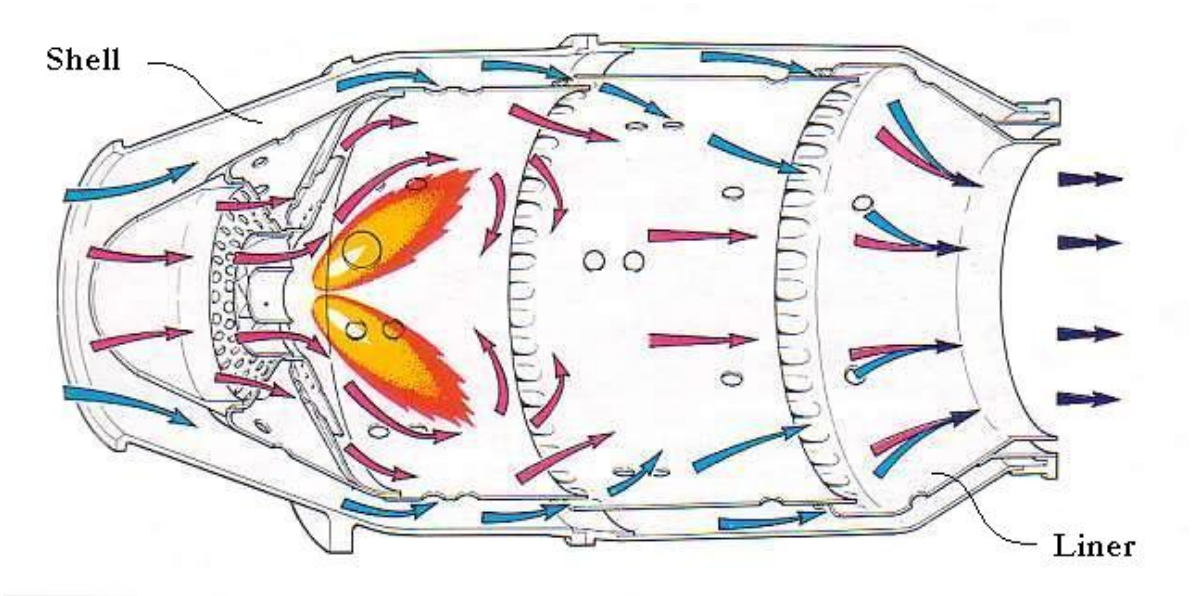

Figure 1: Film Cooled Combustor Liner

1.2 Impingement Cooling

Many engine designers have used jet impingement cooling to achieve the degree of heat removal necessary for backside combustor cooling because of its enhanced heat transfer characteristics. Jet impingement cooling is usually comprised of an array of round jets, which impinge onto the surface to be cooled, known as the *target plate*. Generally, a plate with an array of holes, known as the *jet plate,* produces these impingement jets. The jet Reynolds number, Re_D, is often used to characterize impingement jets and is defined in Eq. 1

$$\mathrm{Re}_D = \frac{UD}{\nu} \quad (1)$$

where U is the average jet velocity at the discharge, D is the hole diameter, and ν is the kinematic viscosity of air. Figure 2 shows a regular array of round impingement jets.

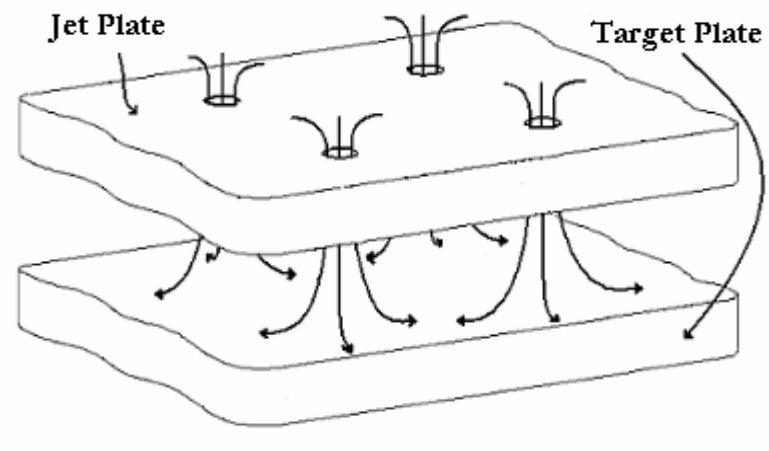

Figure 2: Jet Impingement Array

Figure 3 shows the velocity profile of a single round impingement jet. Usually the jet is fully turbulent at the discharge of the nozzle and has a fairly uniform velocity profile. As the jet moves away from the discharge, it begins to interact with the surrounding air, where momentum diffusion causes the jet to widen. Conversely, the region where the initial uniform velocity is retained, known as the *potential core*, begins to shrink with increasing distance from the jet plate. Eventually, this potential core is completely diffused and the maximum velocity at the jet center begins to decrease. Once the jet reaches a certain point it begins to sense the target plate and this structure transforms. The *free jet* is known as the portion of the jet that is not affected by the target plate[2]. The *impingement zone* is the region of the jet that is influenced by the target plate. The *stagnation point* is the location at the center of the jet contact area, and it is characterized by zero jet velocity.

As the jet spreads in the radial direction, the flow begins to accelerate as it moves away from this stagnation point. This acceleration cannot continue indefinitely because of momentum diffusion with the surrounding flow. Eventually, the jet begins to decelerate until it reaches zero velocity and the jet joins the surrounding air. This region of flow deceleration is known as the *wall jet*[2]. Formally, a singularity of zero heat transfer exists at the stagnation point; however, an experimental realization of this is not realistic. Therefore, experimentalists generally consider the stagnation point the location of maximum heat transfer.

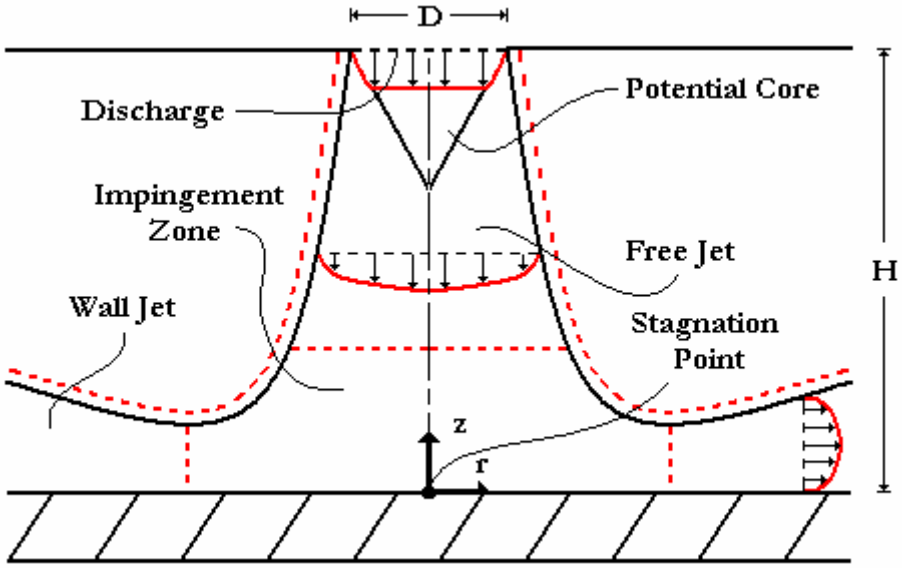

Figure 3: Single Impingement Jet Profile

In large impingement arrays, jet–to-jet interactions significantly deform the ideal jet structure of Figure 3, and substantial degradation in heat transfer occurs. One such interaction is spent air *crossflow*. Figure 4 shows an array of impingement jets under the influence of crossflow.

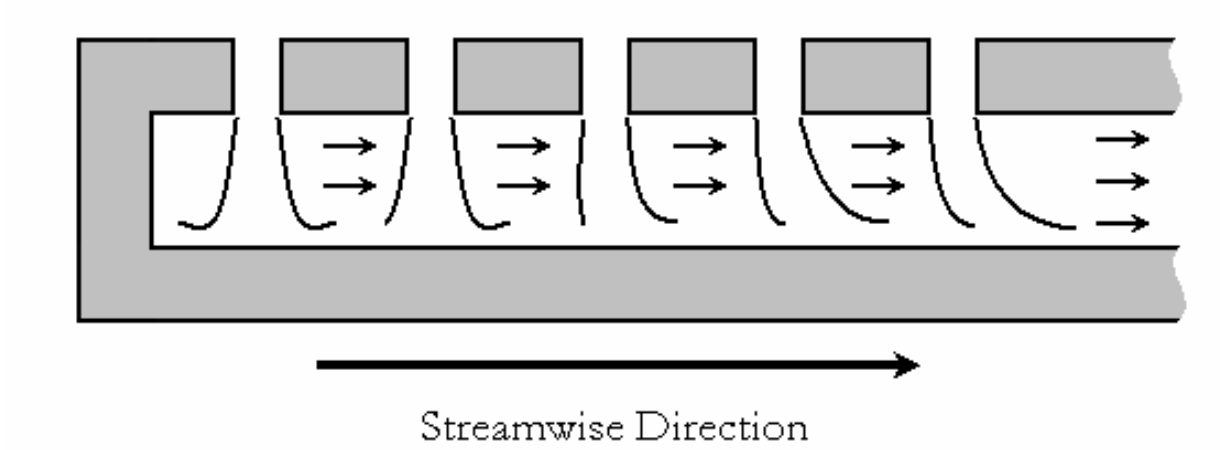

Figure 4: Impingement Array with Crossflow

Crossflow interactions become significant when the exit direction of a large impingement array is restricted to a single direction. In this configuration, spent air from upstream jets must flow across the impingement zone of the downstream jets in the streamwise direction. This pushes the downstream jets away from the target surface, stretches their jet contact area, and reduces the occurrence of a stagnation region. Each of these crossflow consequences leads to large degradations in heat transfer.

1.3 Literature Survey

Researchers have examined many different parameters that affect the performance of impingement jet arrays over the years[3-9]. These studies include investigations into the parametric effects of jet geometry, temperature, crossflow, turbulence, etc. on impingement heat and mass transfer. Down and James[10] performed a comprehensive literature survey of all the jet impingement studies and correlations. Huber and Viskanta[11,12] studied the heat transfer effect of jet-to-jet spacing and jet location for confined arrays of axisymmetric air jets. Van Treuren et al.[13] measured both local heat transfer coefficients and adiabatic wall temperatures under impinging jets. They were the

first to present detailed heat transfer distributions underneath impinging jets and showed maximum heat transfer near the stagnation point.

Kercher and Tabakoff[4] first determined that spent air crossflow adversely affects the heat transfer characteristics of impingement jet arrays. They derived correlations for the effect of crossflow on impingement heat transfer in both inline and staggered hole patterns. Huang et al.[14] also studied the effect of crossflow direction on impingement heat transfer for a square array of jet holes, and determined that heat transfer degradation due to crossflow is minimal when the flow exits in two directions after impingement. Recently, Bailey and Bunker[15] studied the effect of jet array geometry by varying the spacing of a square array of impingement jets. They looked at arrays of spacing, X/D x Y/D, 3 x 3, 6 x 6, and 9 x 9 and also varied the nozzle-to-plate wall distance ratio, H/D, from 1.25 to 5.5. They presented a modification to Florschuetz's[6] correlation. Ekkad et al.[16] presented heat transfer distributions for arrays of spacing 4 x 4, 8 x 8, and rectangular arrays of spacing 4 in the streamwise direction and 8 in the spanwise direction. They also varied their nozzle-to-plate spacing, H/D, from 1 to 5. They showed that closer spacings increase the jet-to-jet interaction and produce higher heat transfer in the regions between jets.

Several documents[17-22] have examined various combustor conditions and their effect on certain emissions. Designs using dilution air and film cooling of various types have also been the focus of several different studies. These techniques are common in aircraft engines where NOx emissions are not considered. Chin et al.[23] were the first to study shingled combustor liners. Various studies have focused on different film cooling geometries. Schulz[24] presents an overview of all the relevant liner cooling methods wherein film cooling alone or in a combination with backside convective cooling was primary research focus.

Many researchers have investigated the heat transfer enhancement capabilities of various turbulence promoters, such as ribs, dimples, and pin fins. Engine designers have used rib turbulators inside airfoils for internal heat transfer enhancement for the past three decades. Several researchers have presented experimentally derived correlations for rib turbulators[25-28]. Experiments

have also shown that dimples can produce significant heat transfer enhancement with very little pressure drop across the dimpled surface. However, Ekkad and Kontrovitz[29] showed that placing dimples on an impingement target surface actually degrades heat transfer. Researchers have examined several other promising methods of heat transfer enhancement; however, most of these techniques required a huge pressure drop or were expensive to manufacture with respect to the present problem.

Studies that examine the backside cooling of combustor liners are few in number. Bailey et al.[30] presented an experimental and numerical study of heat transfer enhancement for backside cooling of a combustor liner. They used impinging jets with rib turbulators downstream of the impingement region. Results show that the rib turbulators enhance heat transfer significantly in the region downstream of the pure impingement, where crossflow would push the impinging jets away from the target surface. Gao et al.[31] and Hebert et al.[32] studied linearly stretched impingement arrays that seem to perform better than conventional square and rectangular arrays under the presence of crossflow. Both the spanwise and streamwise hole spacing was increased in the exit direction providing more area for the spent crossflow to pass through resulting in more localized impingement and thus enhanced heat transfer.

1.4 Experimental Objectives

The primary objective of this two-part study is to examine the application of different impingement configurations to the backside cooling of modern low emission gas turbine combustors. A transient liquid crystal technique will be used to obtain detailed heat transfer coefficient profiles for all test cases. Each part of the study will explore a different way to reduce the detrimental effects of spent air crossflow in impingement cooling schemes. Part I will focus on the combination of trip strips and sparse impingement arrays. The second part of the study will present an innovative impingement configuration, called the *zero-crossflow* design, which has the potential to completely eliminate the negative effects of crossflow by redirecting spent air. Subsequent chapters will discuss each of these test rigs in detail.

C H A P T E R 2

EXPERIMENTAL APPARATUS

Figure 5 shows the overall view of the experimental setup for this study. The test rig was composed of the following components: an air heater, a diverter valve, a plenum, an inlet section, a test section, a data acquisition system, an image processing system, a frame grabber board, and a RGB camera. Air was supplied to the test rig by an in-house compressor. The mass flow rate was set through an orifice meter to produce a desired jet velocity. A solid-state relay based temperature controller and an insulated 1.5 kW in-line air heater maintained a constant air temperature.

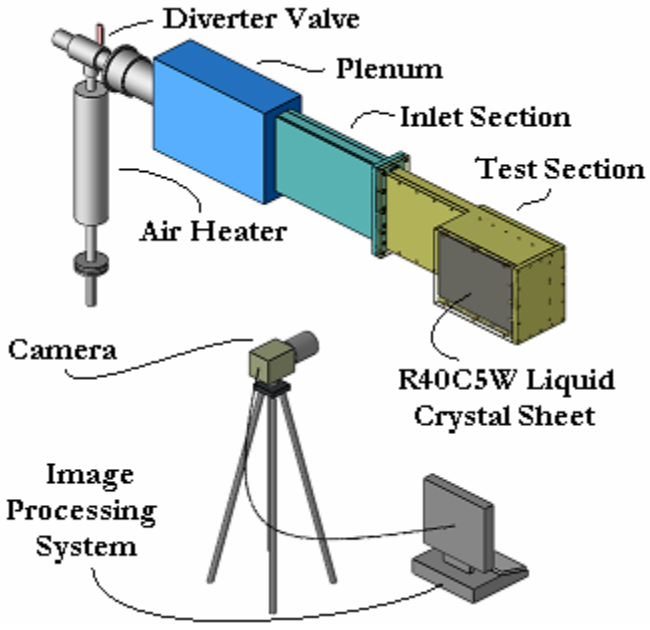

Figure 5: Experimental Set-up

2.1 Flow Conditioning

A high pressure, constant temperature flow rate was required for each test in this study with the most demanding case having a mass flow rate of .1050 kg/s of air. The main-flow also reached fully developed conditions before entering the test section. A three-part flow conditioning system consisting of an in-house compressor, an air heating system, and an inlet section produced these flow conditions. A compressor supplied the constant mass flow of air. The air heating system maintained the flow at a constant temperature, and the inlet section ensured fully developed conditioned were reached. This section will discuss each of the subsystems in detail.

2.1.1 Air Supply

An in-house 290-psi compressor supplied the high-pressure airflow for this study. The compressor was a two-stage, oil-injected screw compressor designed for higher-pressure air applications. A highly efficient TEFC electric motor powered this component.

Figure 6: In-house Compressor

2.1.2 Temperature Control

The air heating system was composed of a solid-state relay based temperature controller, an insulated 1.5 kW in-line air heater, and a diverter valve. These components worked in conjunction to produce the desired mainstream temperature for each experiment. The controller maintained a constant temperature by varying the frequency of on/off cycles of the air heater to obtain the desired condition. The diverter valve directed the air away from the test section during the heating process. The desired mainstream temperature produced by this system varied with each test case and Re_D. Table 1 shows the mainstream temperatures for all test cases and Re_D's in both parts of the study.

Table 1: Mainstream Air Temperatures for All Test Cases

Re_D	PART I				PART II		
	CASE 1	CASE 2	CASE 3	CASE 4	CASE 1	CASE 2	CASE 3
10000	37.8°C	37.8°C	40.5°C	43.3°C	54.4°C	60.0°C	65.6°C
20000	32.2°C	33.9°C	35.0°C	35.0°C	43.3°C	43.3°C	48.9°C
30000	31.7°C	32.0°C	32.2°C	32.2°C	43.3°C	43.3°C	46.1°C

2.1.3 Inlet Section

Figure 7 shows a diagram of the inlet section, which is the final element of flow conditioning before the flow enters the test section. The inlet section is a 2.54 cm x 17.78 cm rectangle channel 45.72 cm long. The highest Re based the hydraulic diameter of this inlet section was 1375. The inlet section was designed with an L/D ratio of 7, which ensured that fully developed conditions were reached before the test section in all cases. Finally, a uniform air temperature was produced by a rectangular plenum that was placed just upstream of the inlet section.

2.2 Test Sections

Each part of this study examined a different impingement scheme. Part I examined impingement enhancement combined with trips strips. Part II studied a new zero-crossflow design.

Each study focused on improving jet impingement characteristics by reducing the effect of spent air crossflow. The following section will discuss these test sections in detail.

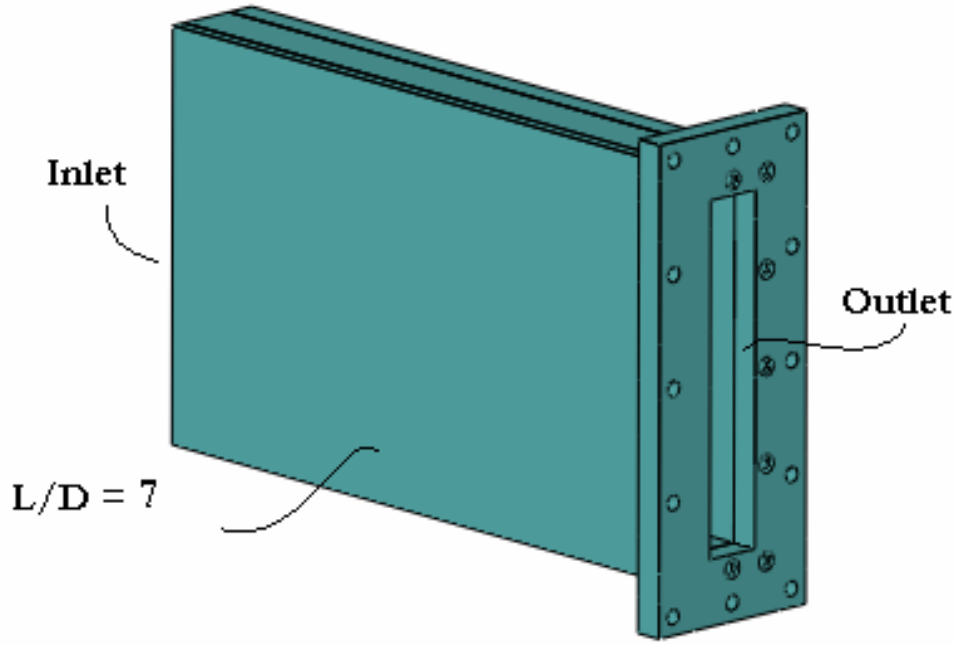

Figure 7: Inlet Section

2.2.1 Part I: Impingement with Trip Strips

The effect of trip strips on the performance of various impingement configurations was the primary focus in this part of the study. Figure 8 shows a cut away view of the test section used in Part I. This test rig consisted of three chambers separated by a .635 cm slotted inlet plate and jet impingement plate oriented parallel to the incoming flow. The first chamber had the same cross-section as the inlet chamber and was 22.86 cm long in the flow direction. The slotted inlet plate allowed air to flow to the second chamber of the test section where it encountered the impingement jet plate. The jet plate directed the flow into the third chamber, the impingement section, producing impingement jets perpendicular to the inlet flow direction towards the 1.27 cm plexiglass test plate.

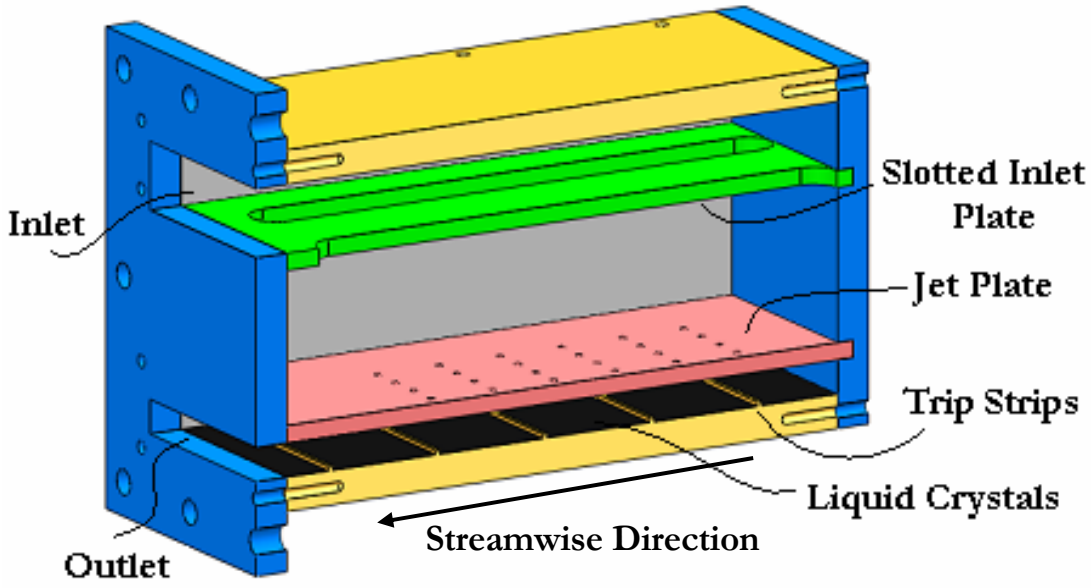

Figure 8: Cut-away of Part I Test Section

The impingement section was a 1.27 cm x 15.24 cm rectangular channel 22.86 cm long. To create adequate crossflow conditions the impingement section had a single outlet, which produced an exit flow in the opposite direction of the incoming flow. This exit direction was called the *streamwise direction*. Additionally, two 1.905 cm x 1.27 cm x 22.86 cm spacers located on the either side of the impingement section aided in the production of crossflow by restricting the flow of spent air. These spacers reduced the impingement chamber cross-section to 1.27 cm x 11.43 cm. The rest of the test section was made of 1.27 cm thick plexiglass. The impingement wall of the test section was coated with a thin layer of thermo-chromic liquid crystals (R30C5W), with a transition to green color at 31.4ºC. Next, a layer of black paint was applied to the liquid crystals to ensure that the colors were visible through the plexiglass wall.

This part of the study examined four different impingement chamber configurations. Figure 9 displays each of these setups. Case 1 studied pure impingement under the presence of crossflow to establish a baseline test for comparison. In all cases, the jet-to-target plate spacing (H/D) was 5,

based on a jet hole diameter of .254 cm. The base jet plate of Case 1 consisted of a rectangular 8 x 11 array with a hole spacing, S/D, of 5 in both directions. In each of the remaining cases, specific rows of holes on the base plate were blocked to produce a different jet array.

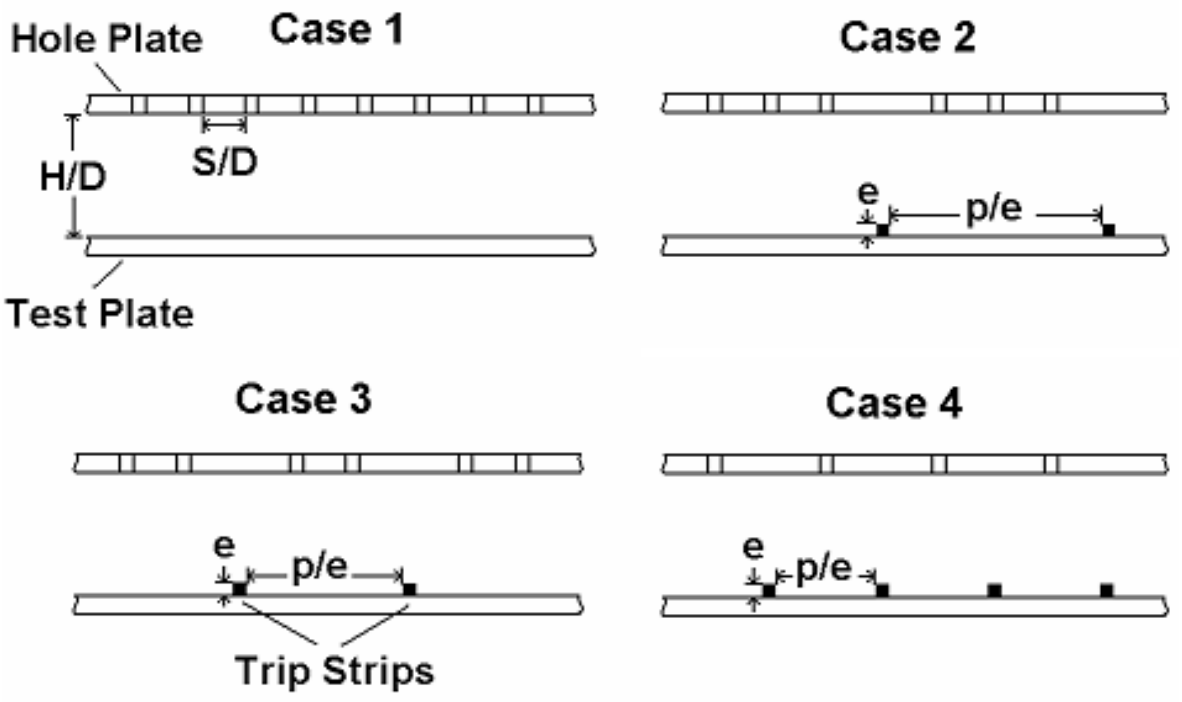

Figure 9: Test Case Configurations

Ribs were placed on the target plate underneath the blocked jets for Cases 2, 3, and 4 to study the interaction of impingement jets and trip strips. The trip strips were square ribs with a height, e, of .15875 cm, and were made of a plastic material of low thermal conductivity. Heat transfer results underneath the ribs were not obtained because of the non-conductive material used to make them. In case 2, every fourth jet row was blocked and a rib was placed on the target surface at the X/L location of the blocked jet row. This produced a rib pitch to height spacing, p/e, of 32. Every third jet row was blocked in Case 3 corresponding to a rib p/e equal to 24. Finally, Case 4 was constructed by blocking every other jet row leading to a p/e spacing of 16.

2.2.2 Part II: Zero Crossflow Impingement

The complete elimination of crossflow effects was the main goal for the second part of this study. The central idea behind this elimination was to design an impingement configuration that provided the spent air an exit path that did not interfere with any impingement jets downstream. This was achieved by constructing channels that protected the impingement jets from any interactions with crossflow. Figure 10 shows a single impingement channel, similar to the ones used in Part II. The coolant enters the top of the impingement trough. The coolant flow passes through the jet plate, then impinges onto the target plate. Next, the air travels up and away from the target plate leaving the downstream impingement jets uninterrupted.

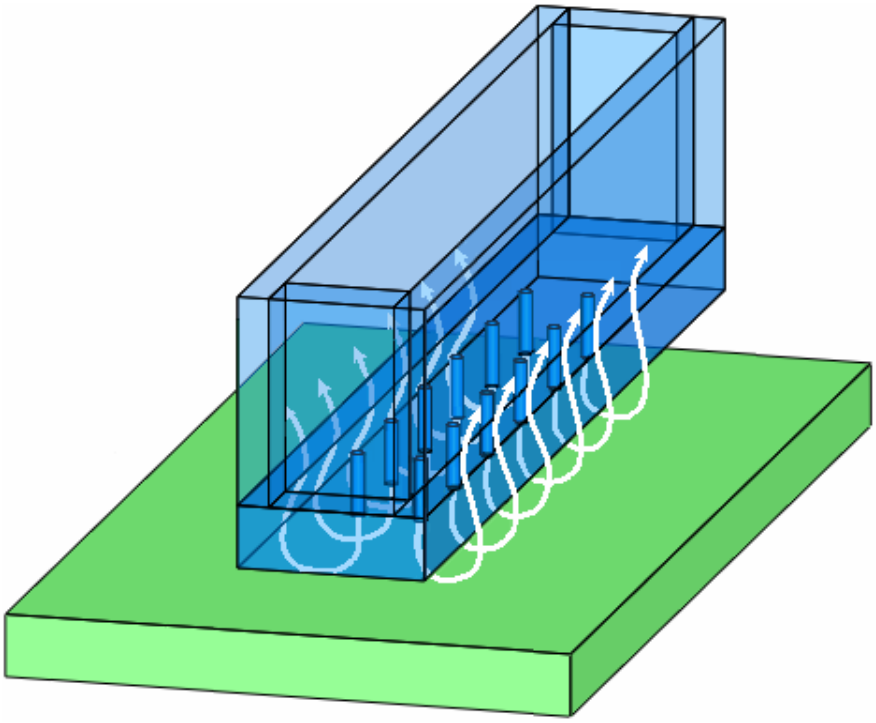

Figure 10: A Single Impingement Channel

Figure 11 shows a cut-away view and Figure 12 shows a cross-section view of the zero-crossflow test rig. In this impingement configuration, three impingement channels extended into the main impingement chamber. After the coolant has impinged upon the test plate, it flowed into the gap between each impingement channel and then out of the test rig without disturbing any downstream jets. The sidewalls of each impingement channel were made of .635 cm plexiglass. The hole plates on the bottom of each impingement channel were made of 1.27 cm plexiglass. An R35C5W liquid crystal sheet with a green color transition temperature of 36°C was placed on the target surface for temperature visualization during testing. The reminder of the test section was identical to Part I, with the exception of a straight channel at the inlet to the test section. This 45.72 cm long channel was made of 1.27 cm plexiglass and had a rectangular cross-section of 2.54 cm x 17.78 cm.

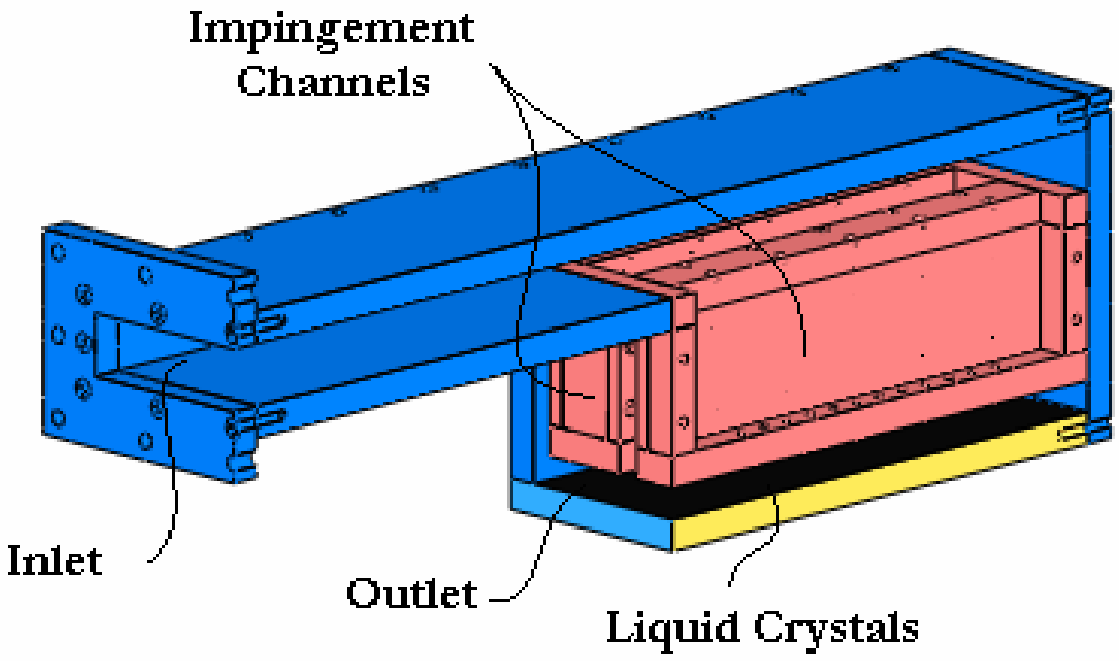

Figure 11: Part II Test Section Cut-away

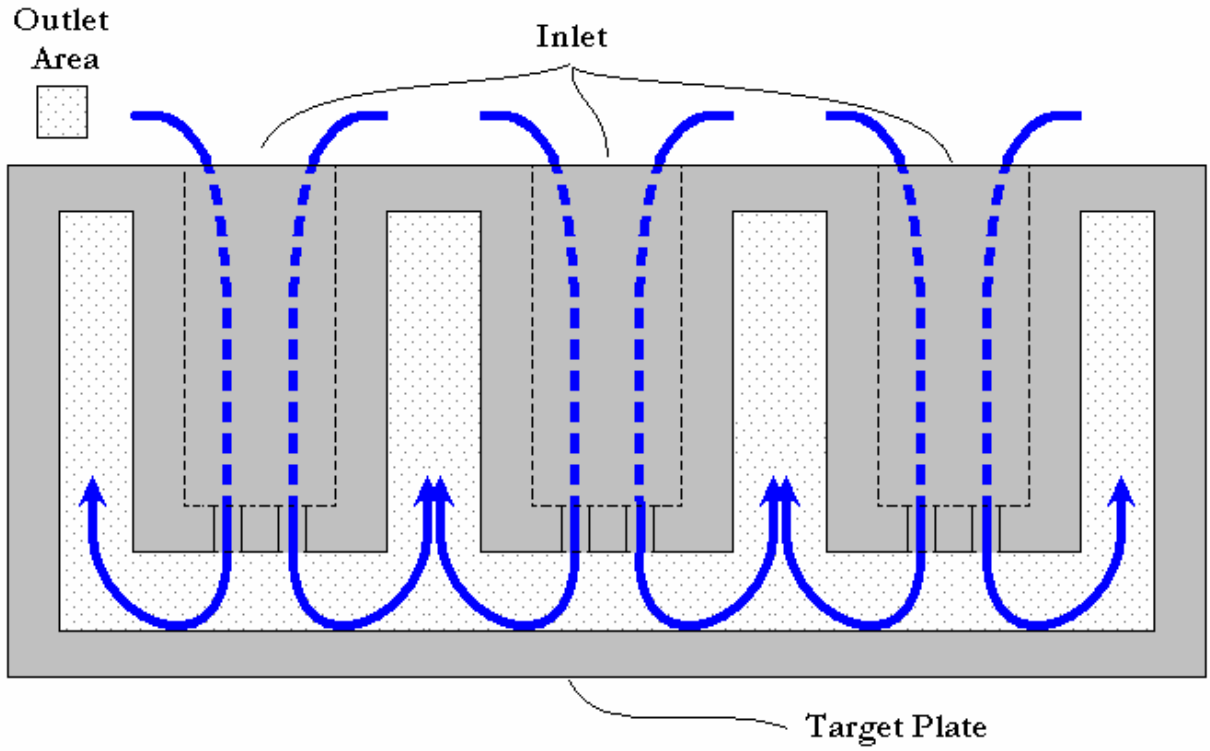

Figure 12: Cross-Section View of Zero-Crossflow Rig

Three different cases were studied in the zero-crossflow design, each having a different hole configuration. These cases were produced by replacing three interchangeable hole plates at the bottom of each impingement channel. Case 1 was a regular 2 x 11 array of .254 cm diameter jet holes with a spacing of 5 hole diameters in the spanwise and streamwise directions. Case 2 was constructed by replacing every other jet row with a single jet hole at the centerline of the plate starting with the first row. Finally, Case 3 consisted of a staggered array of holes with a single hole at every jet row positioned at alternating locations of the Case 1 holes. Figure 13 shows the hole pattern for each test case.

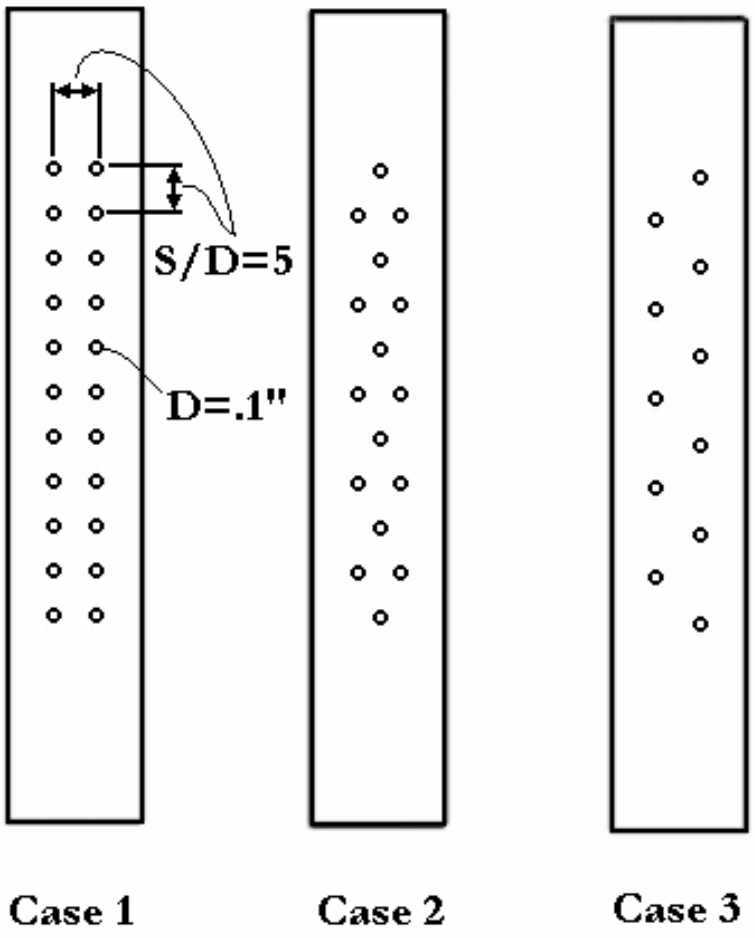

Figure 13: Part II Test Cases

C H A P T E R 3

HEAT TRANSFER THEORY

The determination of local convection heat transfer coefficients was the main goal of this study. The chapter will present the development of a heat transfer model, along with validations of all assumptions made during this process. Finally, the transient nature of the mainstream temperature will be discussed in the last section.

3.1 Steady and Transient Convection

First, consider a simple flat plate flow with a convective boundary condition (BC). Figure 14 shows a diagram of this problem.

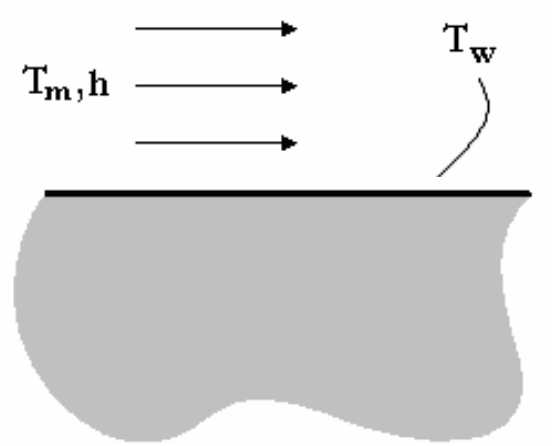

Figure 14: Flow over a Flat Plate

Assuming steady state conditions, an energy balance performed on the plate's outer surface results in Eq. 2.

$$q'' = h\left(T_w - T_m\right) \quad (2)$$

where h is the heat transfer coefficient, q'' is heat flux, T_w is the wall temperature, and T_m is the mainstream temperature. This equation has four variables, thus to compute h one must measure both temperatures and the heat flux at the wall. In some experiments, measuring these temperatures and applying a constant heat flux through heaters is an acceptable way to solve this problem experimentally. However, that choice was not suitable for the present study because the convective BC was on the inner side of the test plate and heaters would have blocked the view of this surface.

Next, consider the transient version of the flat plate flow of Figure 14. In this scenario, the test plate is initially at a uniform temperature, T_i, and the convective BC is instantaneously applied at time, $t > 0$. Now an energy balance performed on the plate results in Eq. 3 with an initial condition (IC) shown in Eq. 4 and a BC shown in Eq. 5

$$\left(\frac{\partial^2 T}{\partial x^2} + \frac{\partial^2 T}{\partial y^2}\right) = \frac{1}{\alpha}\frac{\partial T}{\partial t} \quad (3)$$

$$T = 0 \text{ at } t = 0 \quad (4)$$

$$-k\frac{\partial T}{\partial y} = h\left(T_w - T_m\right) \text{ at } x \geq 0,\ y = 0 \text{ and } t \geq 0 \quad (5)$$

where T is the plate temperature, α is the thermal diffusivity of the wall material, t is time, the y direction is perpendicular to the plate, and x is in the streamwise direction. If heat transfer in the x direction is neglected and only the y direction heat flux is considered Eq. 3 reduces to Eq. 6 with the same IC and BCs.

$$\frac{d^2T}{dy^2} = \frac{1}{\alpha}\frac{\partial T}{\partial t} \qquad (6)$$

Eq. 6 is a second order partial differential equation, therefore one more BC is required to solve T and thus the local heat transfer coefficient, h.

3.1.1 Semi-Infinite Solids

Analytical solutions to the transient conduction problem shown in Eq. 6 are generally limited to relatively simple problems. One such problem is the *semi-infinite solid,* which is any solid that extends to infinity in all but one direction[2]. The semi-infinite solid assumption can also applied to any situation where a thermal wave does not reach the bounds of a solid during the time frame of interest. The application of the semi-infinite solid assumption gives an additional BC, which says at an infinite depth into the plate:

$$T = T_i \text{ at } y = -\infty \text{ for all } t \qquad (7)$$

Eq. 8 shows the resulting solution to Eq. 6 at the wall-fluid boundary of $y = 0$

$$\frac{T_w - T_i}{T_m - T_i} = 1 - \exp\left(\frac{h^2\alpha t}{k^2}\right) erfc\left(\frac{h\sqrt{\alpha t}}{k}\right) \qquad (8)$$

where T_i is the initial temperature of the test surface and k is the thermal conductivity of the wall material. Therefore, with measurements for everything other than h the problem is mathematically closed and heat transfer measurements can be obtained experimentally.

It is important to note that three major assumptions had to be made to obtain an analytical solution for h. The first was that axial conduction was negligible thus only considering conduction in the y direction was sufficient. The second was that the plexiglass test plate behaved as a semi-

infinite solid throughout the duration of the test. The third was that the rig was at a uniform temperature at the beginning of the test. The following sections will address the validity of these assumptions.

3.2 Assumption Validation with Finite Element Analysis

The finite element software package ANSYS was used to examine the validity of the one dimensional conduction and semi-infinite solid assumptions. For this analysis, a 2-D cross-section of the test plate is considered. Let us first consider a cross-section located at the centerline of an impingement jet column along the entire length of the test plate. Figure 15 shows this cross-section with a decaying sinusoidal convective BC, which is typical of the large impingement arrays.

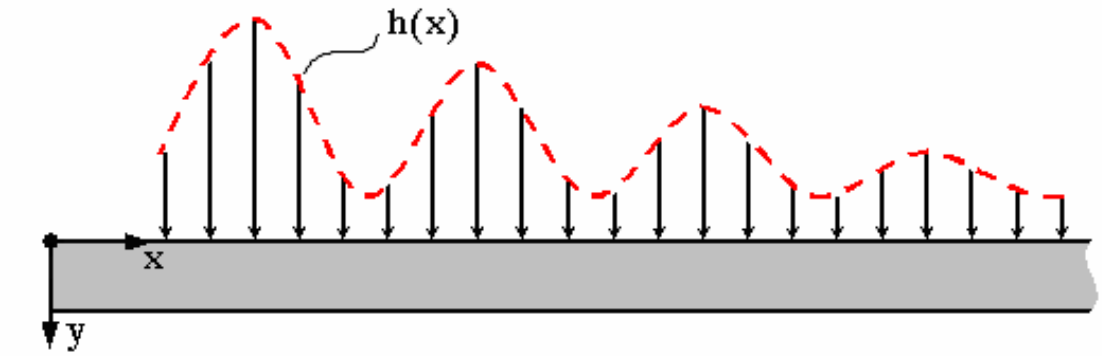

Figure 15: Decaying Sinusoidal BC

The sinusoidal nature of the convective BC applied to the test plate in Figure 15 will produce temperature gradients in the x and y directions. If the thermal gradients in the x-direction are significantly large compared to those in the y-direction, then heat transfer in both directions must be resolved. The greatest possibility for 2-D conduction exists near the upstream impingement jets where the largest variation in h is located. Therefore, if a test plate with a non-decaying sinusoidal BC shows negligible heat flux in the x-direction, then the actual test plate will certainly behave in an equivalent manner. Figure 16 shows the application of a non-decaying sinusoidal BC. The

maximum upstream h variation of the decaying convective BC from the previous model is maintained across the entire plate in this model.

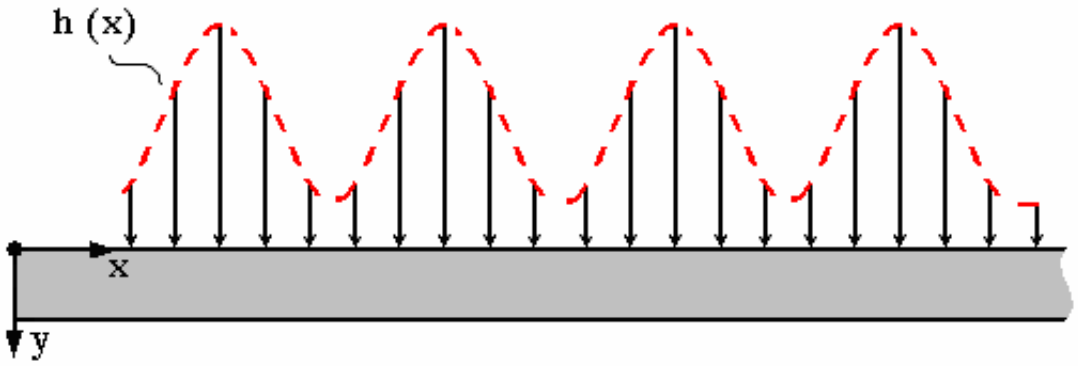

Figure 16: Non-Decaying Cyclic BC

Symmetry planes exist at every h maximum and minimum. Therefore, the problem can be reduced to the heat transfer model shown in Figure 17 by only considering the region of the test plate between a pair of consecutive symmetry planes.

The inside BC of this model is forced convection from impingement with the mainstream flow temperature of 323K and a h profile expressed as a cosine curve fit of experimental data. A free convection BC is applied at the outer surface with an approximate heat transfer coefficient of 25W/m^{2}K and a surrounding temperature of 296K, which is also the initial temperature of the test plate. For the test plate, material properties for plexiglass are used.

3.2.1 The FEA Meshes

Three meshes for this analysis were constructed using decreasing grid sizes resulting in a *coarse*, a *medium*, and a *fine* mesh. The grids were built by specifying the number of nodes along all four edges of the area and connecting them with PLANE77 elements. This element type is an 8-

node quad and was chosen to maximize the total number of nodes while minimizing the number of elements because of computational restrictions.

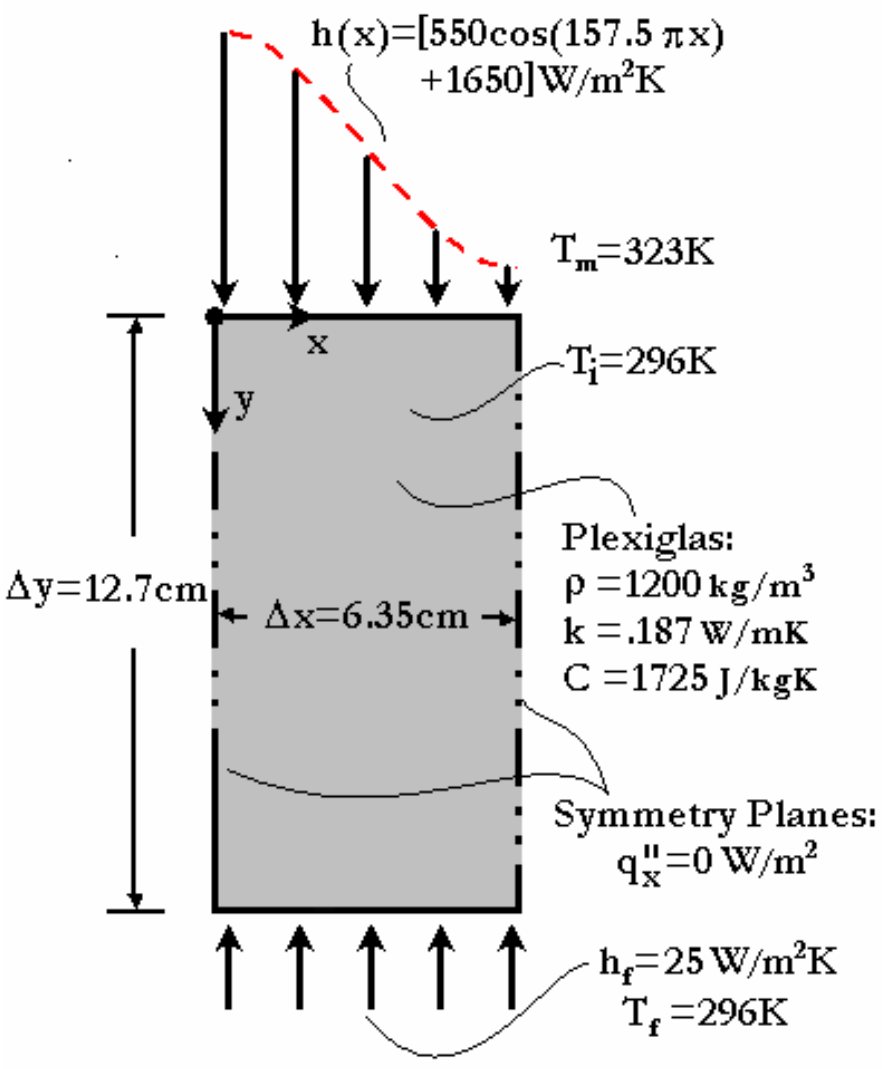

Figure 17: Finite Element Model

The nodes on the top edge were spaced 10:1 from the center to the endpoints. The nodes on the right and left edges were spaced 30:1 from bottom to top, and the bottom edge nodes were spaced evenly. These node spacings were chosen, so the meshes would be tighter near the upper

corners of the area. Figure 18 shows each mesh used in the analysis. Table 2 shows the edge node numbers, N, for each mesh.

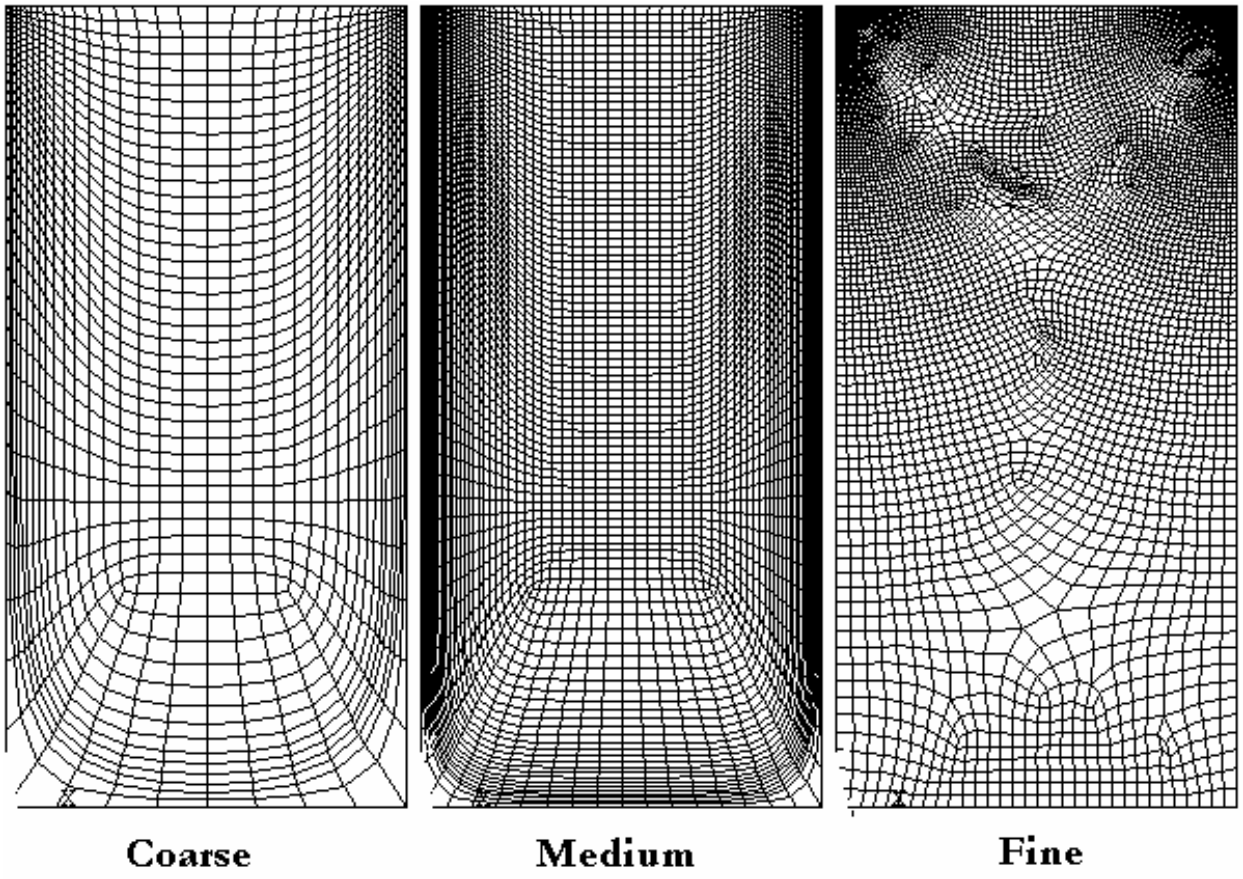

Figure 18: FEA Meshes

Table 2: Edge Node Numbers for Each Mesh

EDGE	N_c	N_m	N_f
Top (10:1)	36	72	144
Right (30:1)	36	72	144
Left (30:1)	36	72	144
Bottom	8	16	32

3.2.2 Time Step Convergence

With the coarse, medium, and fine meshes constructed, the transient thermal analysis of each mesh was carried out at time steps of .05, .1, and .2 seconds to obtain a converged solution in time for each mesh. The transient FEA was performed over a total time interval of 45 seconds, which corresponds to actual test durations. The conduction of heat is a diffusive process, which means gradients in temperature will dissipate as heat passes through a solid. This diffusive behavior means the largest temperature gradients in the test plate will occur at its top surface where heat is initially being transferred to the plate. Therefore, all convergence checks were carried out at the upper edge of the mesh. Three different instances in time (.33sec, 10sec, and 45sec) were examined to ensure convergence was reached throughout the entire test duration. Finally, convergence in both axial and total heat flux was examined at each time step because the ratio of these two magnitudes determines whether axial conduction is negligible. Figure 19 shows total heat flux (THF) at the upper edge of the fine mesh at t=10sec for all time steps. Figure 20 shows the corresponding axial heat flux (AHF) plot.

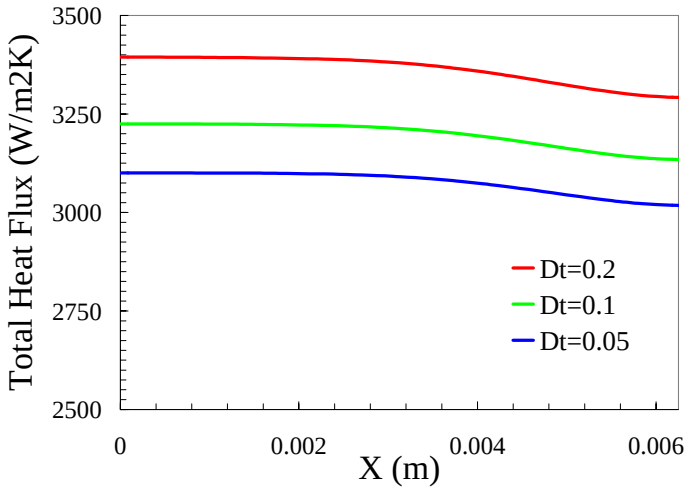

Figure 19: THF at 10sec for Fine Mesh

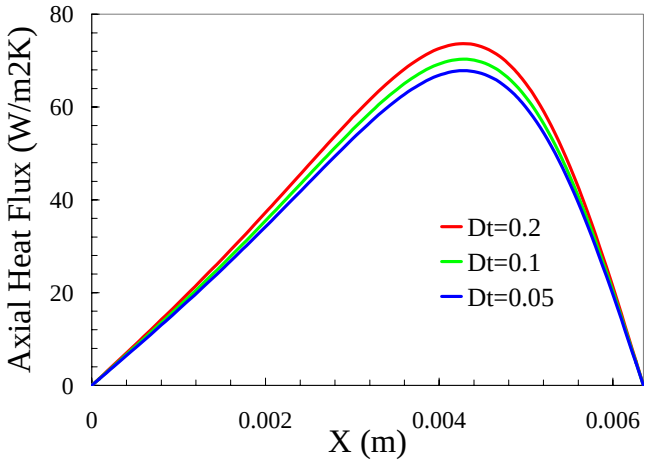

Figure 20: AHF at 10sec for Fine Mesh

A mesh was converging if the difference between sequential time steps was decreasing in this study. If the maximum time step error, $e_{\Delta t}$, defined by Eq. 9, was less than 5% a mesh was deemed converged, where $q_{.05}$ and $q_{.1}$ are the heat fluxes at the .05 and .1 time step, respectively.

$$e_{\Delta t} = \frac{|q_{.05} - q_{.1}|}{|q_{.05}|} \qquad (9)$$

Convergence for total and axial heat flux was reached for the all meshes by the last time step of $\Delta t = .05$. Table 3 shows the maximum time step error for all meshes at each reference time.

Table 3: Maximum Time Step Error

	COARSE		MEDIUM		FINE	
Time	Total	Axial	Total	Axial	Total	Axial
.33sec	3.08%	3.35%	3.22%	1.96%	3.26%	1.49%
10sec	4.05%	4.16%	4.01%	3.84%	4.01%	3.81%
45sec	0.77%	0.80%	1.92%	0.82%	0.80%	0.78%

3.2.3 Discretization Convergence

Comparisons between each mesh size at a given time were performed with time converged solutions for every mesh size. Figure 21 shows the total heat flux on the top edge for each mesh at t=10sec. Figure 22 shows the equivalent axial heat flux plot.

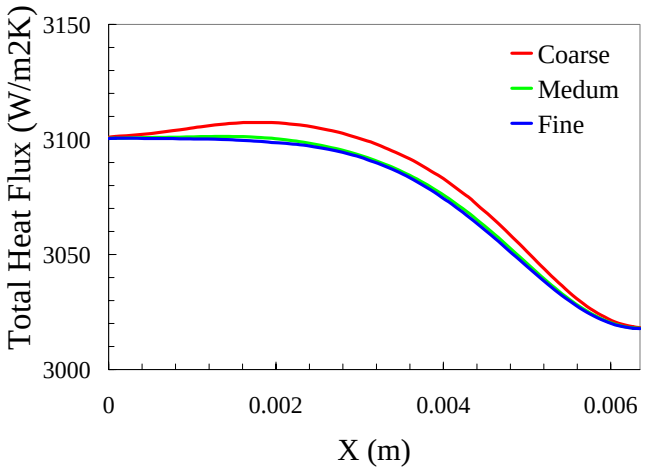

Figure 21: THF at 10sec for All Meshes

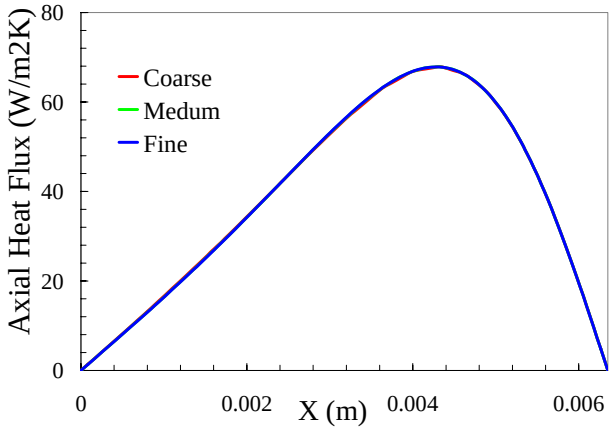

Figure 22: AHF at 10sec for All Meshes

In this part of the FEA study, maximum discretization error, e_d, defined by Eq. 10, is used to judge convergence, where q_f and q_m are the heat fluxes for the fine and medium meshes, respectively.

$$e_d = \frac{\left|q_f - q_m\right|}{\left|q_f\right|} \qquad (10)$$

Again, convergence is clearly reached for both variables. Equivalent convergence was reached at .33 and 45 seconds. Table 4 shows the maximum discretization error at each reference time.

Table 4: Maximum Discretization Error

Time	THF	AHF
.33sec	0.80%	3.26%
10sec	.058%	0.36%
45sec	.22%	0.22%

Finally, with both $e_{\Delta t}$ and e_d obtained for the fine mesh the total error, e_T, could be defined by Eq. 11 as the sum of the time step and discretization errors.

$$e_T = e_{\Delta t} + e_d \qquad (11)$$

The maximum total error along the top edge of the mesh occurred at .33 seconds into the test and was found to be 4.75%, which is within the error level sought of 5%. This total error level signified an adequately converged solution had been reached with an accuracy that surpassed the preset limit.

3.2.4 Key FEA Results

All of the following contour plots show only the upper portion of the plate because the lower portion of the test plate shows little to no change from the initial condition. Figure 23 shows the temperature profiles in the upper half of the fine mesh at t=10sec. Figure 24 shows the total

heat flux at this time value. Slightly higher temperatures and total heat fluxes were seen toward the left side of the plate, which corresponds to the larger convective BC. The axial heat flux behaved in a less intuitive manner. Figure 25 shows the axial contour plots for t=10sec. The AHF reached a maximum value at an axial location just right of the center of the area, which was associated the largest x-direction thermal gradients.

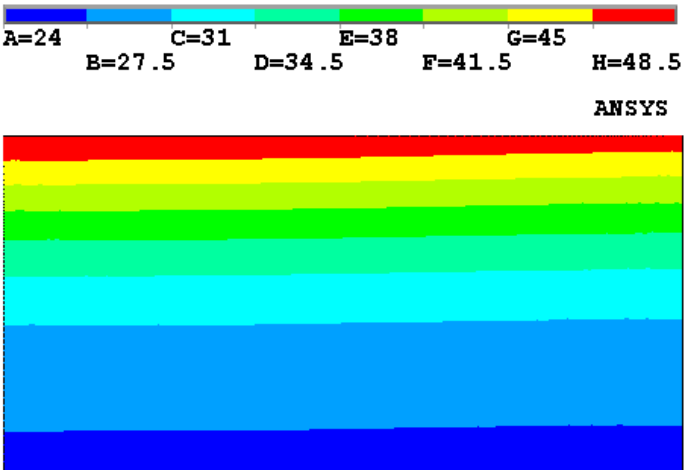

Figure 23: Temperature Profiles at 10 sec.

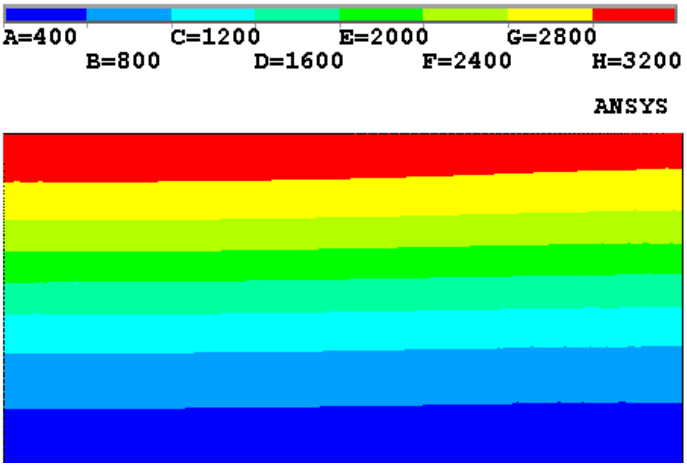

Figure 24: Total Heat Flux at 10 sec.

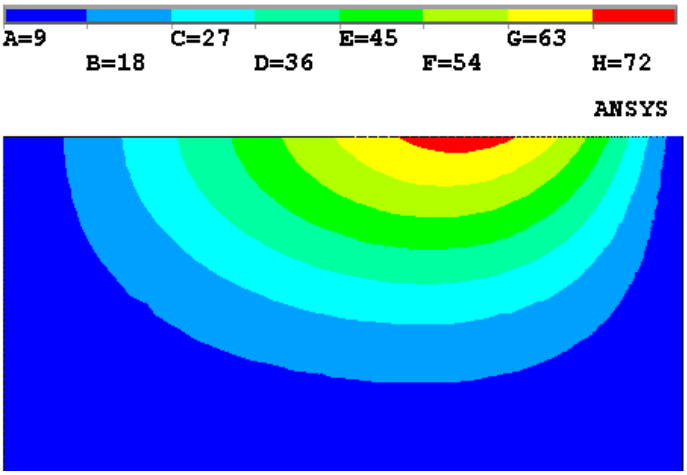

Figure 25: Axial Heat Flux at 10sec

3.2.5 Heat Flux and Temperature Comparisons

The validity of the heat transfer model's assumptions could be addressed with accurate converged solutions for the transient thermal behavior of the test plate. The ratio of axial heat flux to total heat flux was examined along the top edge of the model to judge whether the axial conduction in the test plate was negligible. Figure 26 plots this quantity along the top edge of the test plate for t=.33, 10, and 45 sec. A maximum axial-to-total heat flux ratio of about .022 occurs at t=10 sec. and lasts for the duration of the test, which shows that axial heat flux is clearly negligible for this test configuration.

Comparisons between the temperature profiles through the depth of the plate for the FEA model and analytical semi-infinite solid solution were also performed to determine the validity of the semi-infinite solid assumption. Figure 27 shows this comparison. This temperature plot shows a virtually perfect agreement between the analytical and FEA solution. This concurrence validates the use of the semi-infinite solid assumption in the heat transfer model.

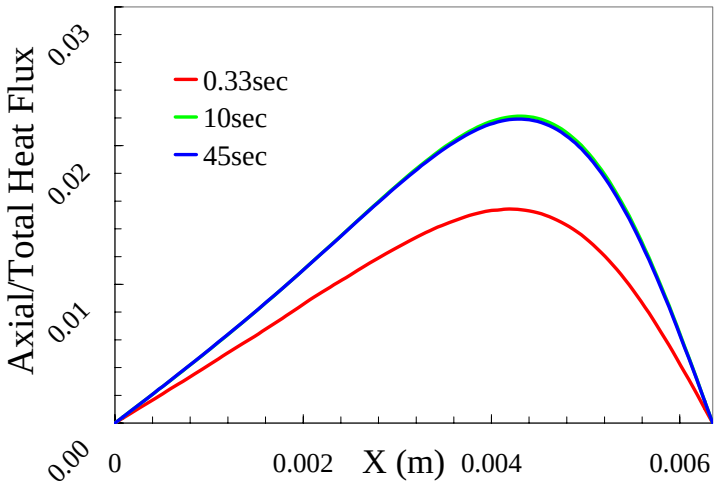

Figure 26: Axial-to-Total Heat Flux Ratios

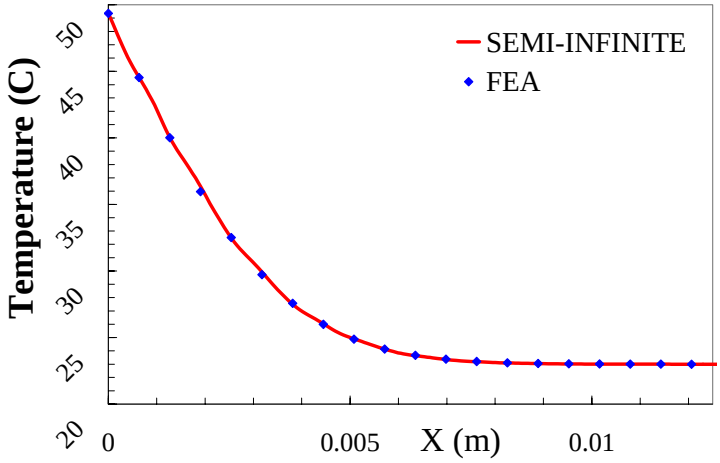

Figure 27: FEA Results and Semi-Infinite Solutions

3.3 Uniform Initial Temperature and Cooling Time

A less-complex 1-D conduction model can be used to determine the amount of time the test rig must be cooled after a test to ensure a uniform initial temperature is reached. An implicit

finite difference technique was used to achieve this goal. The first step in this process was to discretize the test plate. Figure 28 shows a diagram of the discretized plate. Three different types of nodes were employed in this discretization: an upper end node with a convective BC from impingement, middle nodes, and a lower end node with a naturally convective BC from the surroundings.

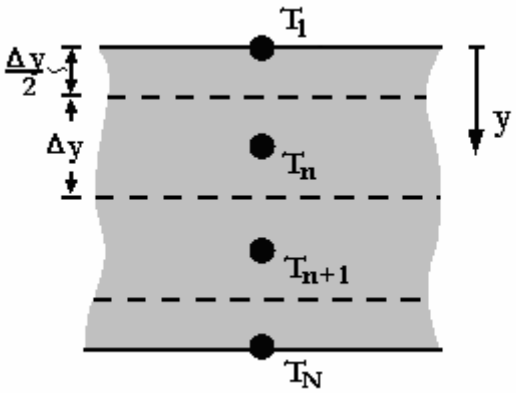

Figure 28: Discretized Test Plate

Figure 29 shows a drawing of the upper node of the test plate with its applied BCs. Figure 30 shows the middle nodes, and Figure 31 shows the lower end node.

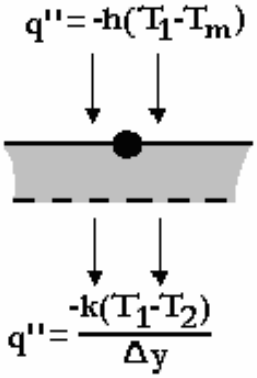

Figure 29: Upper End Node of Test Plate

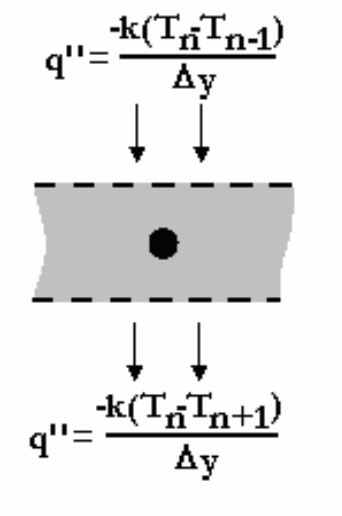

Figure 30: Middle Node

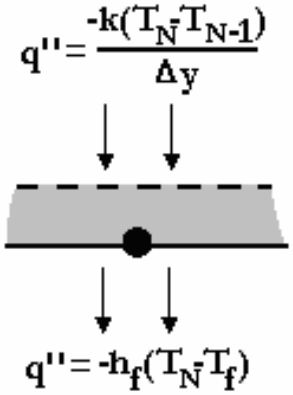

Figure 31: Outside Node

Eqs. 12-14 for the time dependent nodal temperatures were obtained by performing an energy balance on the each node type using finite difference derivatives for space and time.

$$T_1^{\,t+\Delta t} = \left[\frac{\Delta t}{\rho C} \left(\frac{k}{\Delta y} \left(T_1 - T_2 \right) + h \left(T_1 - T_m \right) \right) + T_1 \right]^t \qquad (12)$$

$$T_n^{\,t+\Delta t} = \left[\frac{k \Delta t}{\rho C \Delta y^2} \left(T_{n-1} - T_{n+1} \right) + \left(1 - 2 \frac{k \Delta t}{\rho C \Delta y^2} \right) T_n \right]^t \qquad (13)$$

$$T_N^{\,t+\Delta t} = \left[\frac{\Delta t}{\rho C} \left(\frac{k}{\Delta y} \left(T_{N-1} - T_N \right) + h_f \left(T_N - T_f \right) + q \right) + T_N \right]^t \qquad (14)$$

where Δt is the time step between iterations, Δx is the node size, ρ is the density of plexiglass, C is the specific heat of plexiglass, $T_n^{\,t}$ is the nodal temperature at the nth node at the tth time step, h_f is the free convection heat transfer coefficient from the surroundings, and T_f is the temperature of the surrounding air.

A MATLAB program was written to solve for the time dependent behavior of each nodal temperature. The manner in which the MATLAB code solved for the temperature signals is as follows. The initial state of the model was set as a uniform temperature of 296K before the test starts. Actual heat transfer coefficients obtained from experiments were used as the internal convective BC from impingement. The maximum h for a test case was used for this BC because this is the location of the greatest thermal penetration into the test plate. The free convection coefficient, h_f, at lower end node was set to 25 W/m^{2}K with the surrounding air at 296K. The model was then run for an average test duration of about 45 sec. Figure 32 shows the temperature profiles of such a test, where both the numerically derived solution and the analytical semi-infinite solid solution are plotted. The perfect agreement of the analytical solution and the numerical solution should be noted. This should be expected because the thermal wave has not penetrated the test plate.

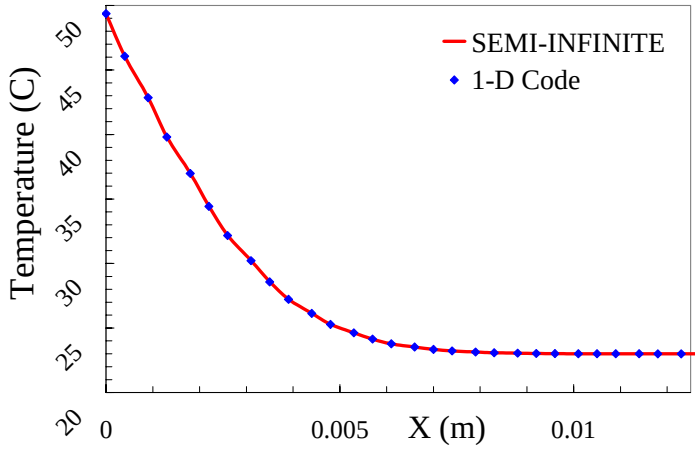

Figure 32: Temperature Profiles after 60 sec

The mainstream temperature was changed to the initial temperature to simulate the cooling period after a test after the heating portion of the numerical analysis was complete. The program was run until the maximum temperature in the plate was within .1°C of the initial uniform temperature. Figure 33 shows temperature profiles for 5, 10, and 21.7 minutes into the cooling process. The inner temperature quickly approached the ambient temperature, then the cooling process was limited by the thermal diffusivity of the plexiglass test plate and the free convection to the surroundings. On average about 20 minutes was found to be a suitable cooling time to ensure uniform temperature; however, around 30-45 minutes was generally used as a precautionary time.

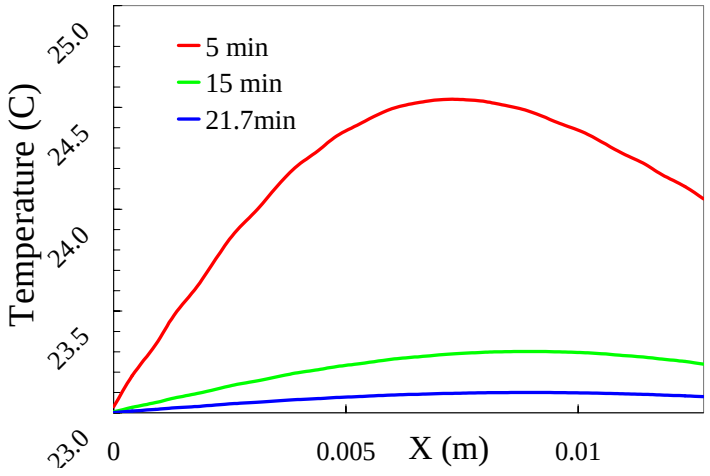

Figure 33: Temperature Profiles at 5, 10, and 21.7 min

3.4 Duhamel's Superposition

The transient behavior of the mainstream temperature can now be addressed with the proven validity of all three assumptions of the heat transfer model .The thermal analysis presented in previous sections of this chapter assumed that the convective BC from impingement was instantaneously started at time, $t > 0$ with a step change in mainstream temperature. The actual mainstream temperatures recorded throughout this study showed a gradual rise in temperature. This was due to heating of the test rig and the thermocouple time constant. The extent of this deviation depended on the Re_D being tested because of the effect of air velocities on thermocouple time constants. To account for this behavior the time dependent temperature signal was broken up into a series of small step changes in time (τ_j , $j = 1,.., N$) as shown in Figure 34.

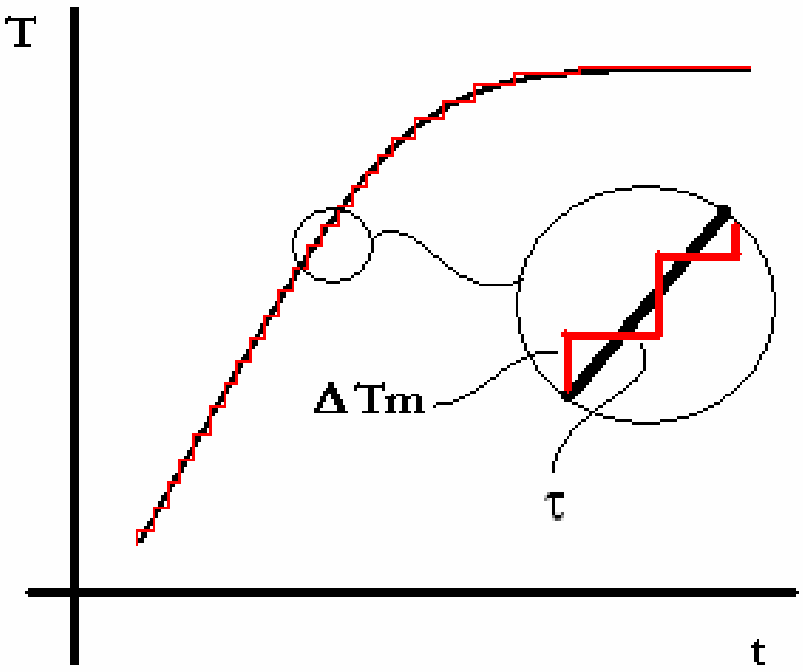

Figure 34: A Discretized Temperature Signal

Using Duhamel's superposition and the evolution of wall temperature given in Eq. 8, the final equation for local h can obtained. Eq. 15 shows this result

$$T_w - T_i = \sum_{j=1}^{N}\left[1-\exp\left(\frac{h^2\alpha(t-\tau_j)}{k^2}\right)erfc\left(\frac{h\sqrt{\alpha(t-\tau_i)}}{k}\right)\right]\left[\Delta T_{mj}\right] \quad (15)$$

where τ_j is the small time step and ΔT_{mj} is its associated mainstream temperature step. With this equation, local h throughout the test surface can be obtained by making measurements of the following quantities:

- The initial temperature of the test rig, T_i.
- The transient mainstream temperature, $T_m(t)$. (Where τ_j is the time between discrete temperature points of $T_m(t)$ and ΔT_{mj} is the temperature difference of those points.)
- The wall temperature, T_w, and the time, t, when that temperature was present.

C H A P T E R 4

EXPERIMENTAL METHODOLOGIES

In Chapter 3, an equation was developed that gives the local h in terms of measurable quantities throughout the test rig. These variables consisted of initial temperature, mainstream temperature, wall temperature, and the time from the initiation of the test to the appearance of the wall temperature. A transient liquid crystal technique was employed to measure the wall temperature and the heating time. The initial and mainstream temperatures were measured with thermocouples and a data acquisition (DAQ) system. This chapter will discuss these methods in detail.

4.1 Liquid Crystal Fundamentals

Thermo-chromic liquid crystals have the unique ability to reflect different wavelengths of light at different temperatures. They accomplish this feat by reflecting only one specific wavelength of visible light at every distinct temperature over a specified range. Liquid crystal formulas can be manufactured with many different initial color change temperatures and many different ranges, or bandwidths. In this study, two different liquid crystal mixtures were used. In Part I, R30C5W liquid crystal paint was used, that had an initial color change temperature of 30°C, a 5°C color change bandwidth, and a green color temperature of 31.4°C. In Part II, R35C5W liquid crystal sheets were used with an initial color change temperature of 35°C, a 5°C color change bandwidth, and a green color temperature of 36°C. In both parts the liquid crystals were placed on a black background.

4.2 Single Color Capturing Technique

In this transient liquid crystal technique, a single color band is tracked for the duration of a test. During the experiment, the time of appearance of the specified color from the initiation of the

test is recorded throughout a region of interest (ROI). Figure 35 shows the image processing system used to accomplish these measurements.

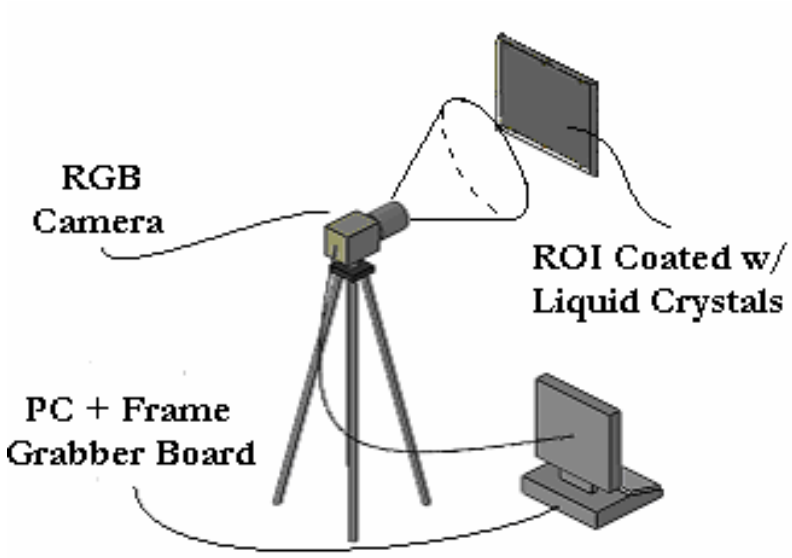

Figure 35: Image Processing System

The image processing system was made up of an RGB camera, a computer (PC), and a frame grabber board. A Pulnix RGB camera with a resolution of approximately 100,000 pixels was used to video the ROI during the test. The frame grabber board was used to digitize each image from the analog camera. The frame grabber board was embedded into the PC through an expansion slot and was controlled by the software package OPTIMAS (v. 6.5). The PC processed each digital image from the frame grabber through an OPTIMAS macro written specifically for this technique.

The RGB camera was focused at the start of each test, and the color band of interest was selected in OPTIMAS. For this study the band of interest was Green, since it is the brightest of the three color bands: Red, Green, and Blue. To track the appearance of Green the absence of this color had to be quantified by the image processing system. Stating that Green was not present when the Green intensity of an image was zero was not an option. Even though black paint was applied to back of the liquid crystals, the black background of the ROI was not a true black surface,

therefore a Red, Green, and Blue color component existed in the ROI even when the surface was visually black. Therefore, the Green intensity of the black background had to be examined before each test. The background intensity was dependent on even lighting of the test section and if lighted properly was fairly uniform throughout the ROI. The maximum background intensity was set as the *threshold*. Choosing the correct threshold value was a crucial part in each experiment. Correctly setting this value meant that during the transient test the green intensity of a pixel would surpass the intensity threshold only if the color Green was actually present. Threshold values between 100-120 were used in this study. Finally, the time in which the color Green appeared, or more specifically the time when the threshold was surpassed, was recorded for each pixel in the ROI.

4.3 Temperature Acquisition

The initial temperature of the test rig and the mainstream temperature throughout each experiment also had to be measured for each test. To accomplish this task thermocouples were used in conjunction with a DAQ system. Both temperature values were sensed using K- type thermocouples. The DAQ system that was used is called *InstruNet*. It read the microVolt outputs of the thermocouples, which were linked to a PC through an *InstruNet* interface. An external terminal box was the connection point for the thermocouples. This apparatus contained signal conditioning amplifiers and cold junction compensators for each channel. It could be configured to convert instrument voltages into several different types of engineering units. For this study, the *InstruNet* system recorded the temperature at a set frequency of 4 Hz.

4.4 Experimental Procedure

The experimental procedure employed for every test in this study is as follows:

1. Set the total coolant flow rate depending on the desired jet Re_D.
2. Direct the coolant flow away from the test section through the diverter valve.
3. Set the temperature controller to the required mainstream temperature.

4. Initialize the temperature DAQ system.
5. Start the image processing macro.
6. Choose a filename for the color transition time file.
7. Choose the region of interest in the image processing software.
8. Choose the background intensity threshold.
9. Begin the image processing system countdown.
10. Direct the coolant flow into the test section at the end of the countdown and start the DAQ system.
11. Wait until the entire region of interest turns green or for 60 seconds, which ever comes first.
12. Stop the DAQ and image processing systems.
13. Turn of the heater and wait the required cooling time until next test can be run.

After each test was performed a temperature data file and a color transition time file were produced. These two files were then input to a FORTRAN program to solve for the local h profiles throughout the ROI. The data reduction program used the bisection method to obtain the heat transfer solutions. Finally, TECPLOT was used to triangulate the finite number of data points into color contour plots.

4.5 Uncertainty Analysis

Experimental uncertainty is an important parameter and must be discussed and quantified in any study. The uncertainty method developed by Kline and McClintock is commonly regarded as the standard method for determining experimental uncertainty. The average experimental

uncertainty for this study can be determined by considering the uncertainty of each individual measurement that must be made to obtain a value of the heat transfer coefficient. These individual measurement uncertainties are as follows:

- Color Transition Time: ± .5 sec
- Mainstream and Initial Temperatures: ± 1°C
- Liquid Crystal Color Change Temperature: ± .2°C
- Material Properties of Plexiglass: ± 6.9%

Using these values, the average uncertainty in the measurement of local h was found to be about ± 6.9%.

C H A P T E R 5

HEAT TRASNFER RESULTS

5.1 Part I: Sparse Impingement Arrays and Trips Strips

The heat transfer tests for all cases in Part I were performed at Reynolds numbers of 10000 (10k), 20000 (20k), and 30000 (30k) based on jet hole diameter. Four different test cases were examined in this part of the study. The total mass flow rate needed to produce the desired Re_D varied in each configuration because the total number of holes was different for each case. Table 5 shows the mass flow rate of air for every test in Part I.

Table 5: Mass Flow Rate of Air in kg/s for All Tests of Part I

Re_D	CASE 1	CASE 2	CASE 3	CASE 4
10000	.0350	.0286	.0254	.0191
20000	.0700	.0572	.0509	.0382
30000	.1050	.0859	.0763	.0572

Figure 36 shows contours of the non-dimensional heat transfer variable, Nusselt number, for each case and Re_D. The Nusselt number based on jet hole diameter, Nu_D, iss defined in Eq. 16.

$$Nu_D = \frac{hD}{k} \qquad (16)$$

where h is heat transfer coefficient, k is thermal conductivity, and D is jet hole diameter.

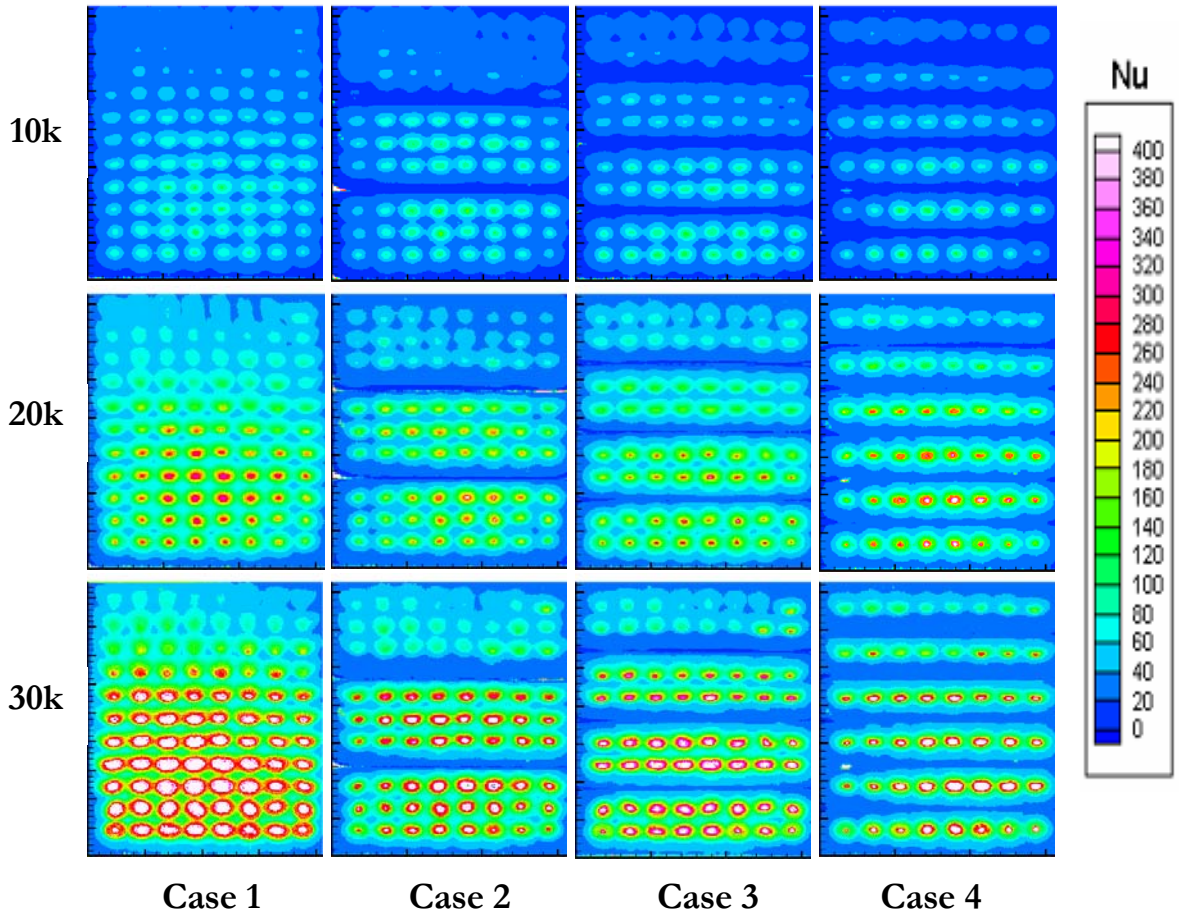

Figure 36: Detailed Nu_D Distributions for Part I

The streamwise, or exit flow direction, was upward for all Nu_D distributions in Figure 36. In every test, high heat transfer regions underneath the impingement jets were clearly visible. However, as the spent airflow increased towards the exit, the heat transfer underneath the jets decreased due to crossflow. This degradation occurred downstream as the crossflow began to push the jets away from the target surface. This behavior was most apparent in Case 1 and high Re_D's. As ribs were added, the number of impingement holes was reduced. Also, the spent air was forced to flow over the ribs causing flow separation and reattachment around the downstream impinging jets. This appeared to reduce the deflection of jets from the target surface resulting in higher heat transfer for the downstream jet locations compared to Case 1. Another reason crossflow degradation was

decreased is that while the jet Re_D was maintained in each case the total coolant flow decreased, thus the amount of crossflow was also reduced. The increase in downstream impingement heat transfer increased as the number of ribs increased from Case 2 to Case 4.

5.1.1 Case 1

Figure 37 shows the spanwise averaged Nu_D distributions for Case 1. The results are plotted against normalized distance, X/L where X is the local streamwise location along the target plate and L is length of the plate. An increase in jet Re_D showed a substantial increase in average Nu_D as expected. The effect of crossflow on the impingement configuration of Case 1 was immediately evident. The upstream jet rows showed peaks of high heat transfer with a maximum located at the fourth jet row, while considerable impingement degradation was seen downstream. Regions of large Nu_D's were present underneath the upstream jets with the area between the rows showing significantly lower heat transfer typical of impingement cooling. This impingement phenomenon was greatly reduced downstream where very little difference in heat transfer was seen between the area underneath and the area between jet rows. This fact shows that the impingement jet structure was greatly deformed downstream because of increased spent air accumulation in the streamwise direction. This jet deformation caused the jet contact area to become stretched in streamwise direction. A shift in the peak heat transfer zone was first realized at the forth jet row and increased in displacement in the streamwise direction. This crossflow induced deflection reached a maximum of approximately 2.9 hole diameters at the last jet row for all Reynolds numbers.

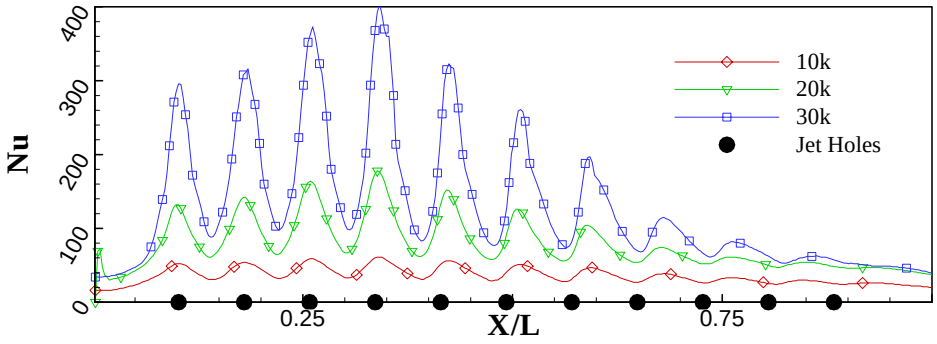

Figure 37: Spanwise Averaged Nu_D for Case 1

5.1.2 Case 2

Figure 38 presents the spanwise averaged Nu_D distributions for Case 2. The number of impingement jets in this configuration was lowered from 88 to 72, thus the total coolant flow rate was decreased by a factor of 1.2. Just as in Case 1, higher jet Re_D's produced higher Nu_D distributions. In this configuration, the negative effects of crossflow were slightly improved. This improvement was quantified by comparing jet contact displacement for each Re_D. For Case 2, the peak Nu_D shift in the streamwise direction was 2.10D, 1.92D and 1.75D for Re_D's of 10k, 20k, and 30k, respectively. These improvements in crossflow interactions occurred for two reasons. First, the presence of trip strips between each three-row section of impingement jets guarded against negative jet interactions. The trip strips directed the crossflow away from the target plate and closer to the discharge of the hole plate where the jets were more powerful and harder to deform. Secondly, less crossflow was present in this configuration, because a lower coolant flow was used while the same jet velocities as Case 1 were maintained.

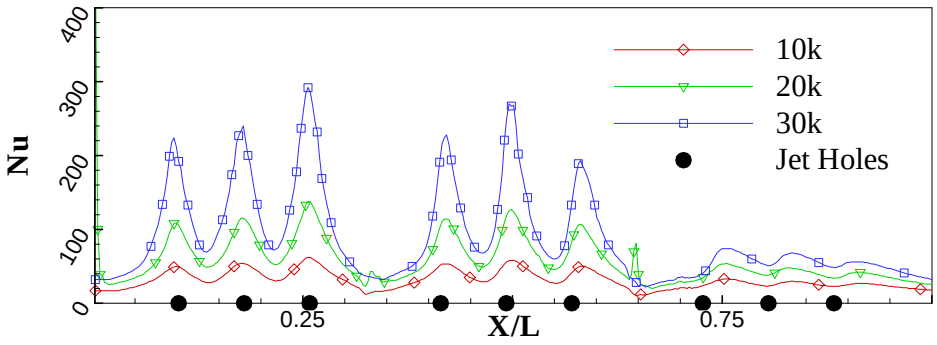

Figure 38: Spanwise Averaged Nu_D for Case 2

5.1.3 Case 3

Figure 39 presents the spanwise averaged Nu_D distributions for Case 3. In this situation there were 64 impingement jets leading to a total coolant flow rate about 1.4 times smaller than Case 1 for all Re_D's. This configuration had a trip strip between each two-row section of impingement jets. Further reductions in crossflow and impingement jet interactions were realized in this set-up

because of an increase in the number of trip strips and an additional decrease in coolant flow. This improvement correlated to a Nu_D displacement of approximately 1.75D for all jet velocities tested.

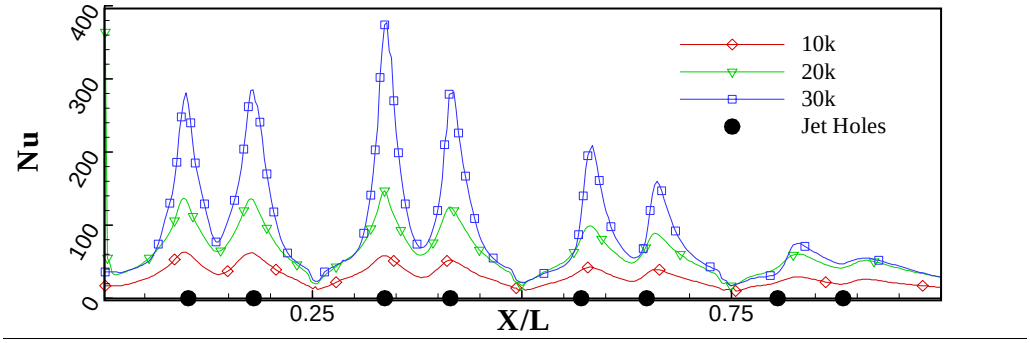

Figure 39: Spanwise Averaged Nu_D for Case 3

5.1.4 Case 4

Figure 40 presents the spanwise averaged Nu_D for Case 4, which exhibited greatly diminished crossflow effects. In this situation, six impingement jet rows spaced 10-hole diameters apart in the streamwise direction were protected by trip strips located between each jet row resulting in a total of five ribs. Also, the total coolant flow rate was further reduced to 54.5% of the flow rate of Case 1. These configuration changes resulted in a maximum jet contact displacement of only 1.25D. Additionally, much greater differences in Nu_D were seen underneath and between downstream jets in Case 4, which showed far less impingement jet deformation than previous cases.

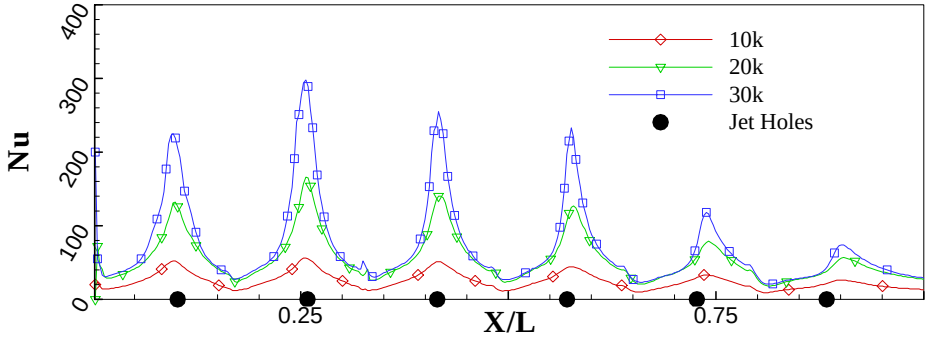

Figure 40: Spanwise Averaged Nu_D for Case 4

5.1.5 Area Averaged Nusselt Numbers

Figure 41 presents the area averaged Nu_D's computed for all test cases in Part I. In this plot, the test cases with the largest coolant flow rates, namely all Re_D's of Case 1, showed the greatest degree of heat transfer. However, it should be noted that Case 4 showed approximately 65% of the cooling capability of Case 1 with only 54.5% of the coolant flow for all Re_D's. It should also be noted that the trip strips used in this study were non-participatory ribs; therefore, underneath the trip strips no heat transfer data was collected. It has been shown by several researchers[25-28] that on-rib regions have substantially larger heat transfer coefficients than their surrounding area. This fact would increase the effectiveness of Case 4, because five ribs existed in this configuration compared to no ribs for Case 1. The same effect would be seen in Cases 2 and 3, but the additional effectiveness would be less significant.

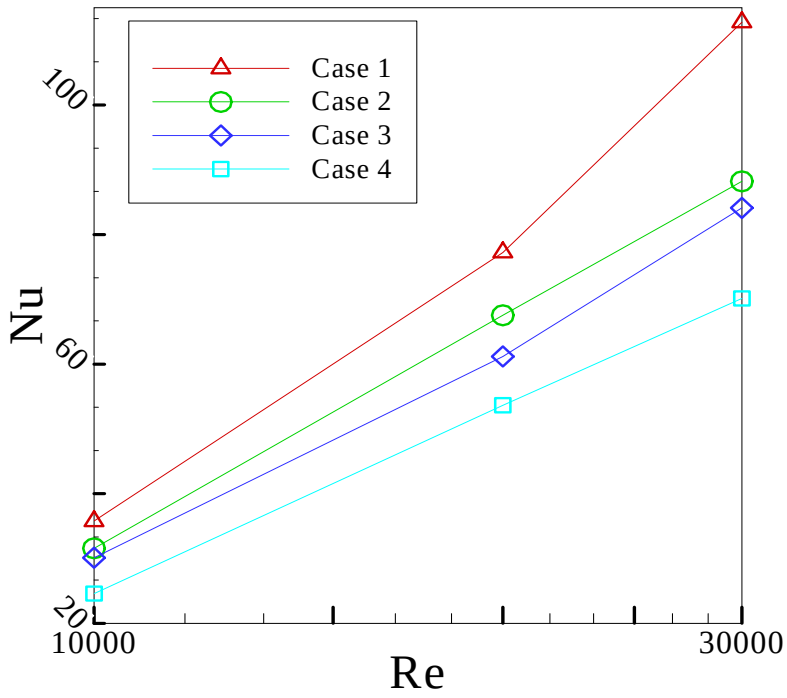

Figure 41: Area Average Nu_D of Part I

5.2 Part II: Zero-Crossflow Design

Jet Reynolds numbers of 10k, 20k, and 30k were also examined for each test case in Part II, however only three different test cases were examined in this part of the study. Again, the total mass flow rate for each configuration changed. This mass flow variation was also due to changes in the number of impingement jets in each test. The mass flow rate of air for every case and Re_D in Part II is shown in Table 6.

Table 6: Mass Flow Rate of Air in kg/s for All Tests in Part II

Re_D	CASE 1	CASE 2	CASE 3
10000	.0262	.0202	.0131
20000	.0524	.0404	.0262
30000	.0786	.0606	.0393

Figure 42 shows the detailed Nu_D distributions for the center trough of each test case. Just as in Part I, high heat transfer regions occurred near the jet stagnation point, which increased with increases in jet Re_D. However, in these impingement configurations heat transfer degradation in the streamwise direction due to crossflow was all but eliminated. Very little contact area stretching in the streamwise direction occurred in Case 1, and the jets with highest Nu_D shifted toward the center of the impingement channel. Actually, a little jet stretching in the spanwise direction was realized in this configuration, which shows that the spent airflow was being directed into the regions between the impingement troughs as intended. The overall effect of these crossflow improvements was that fairly uniform heat transfer was achieved for the majority of the coolant jets in every impingement configuration. In fact, the Nu_D profiles displayed in Figure 42 are practically symmetric about a spanwise axis at the mispoint of the test plate. This symmetric pattern shows that the exit flow direction had little to no effect on the heat transfer of downstream jets.

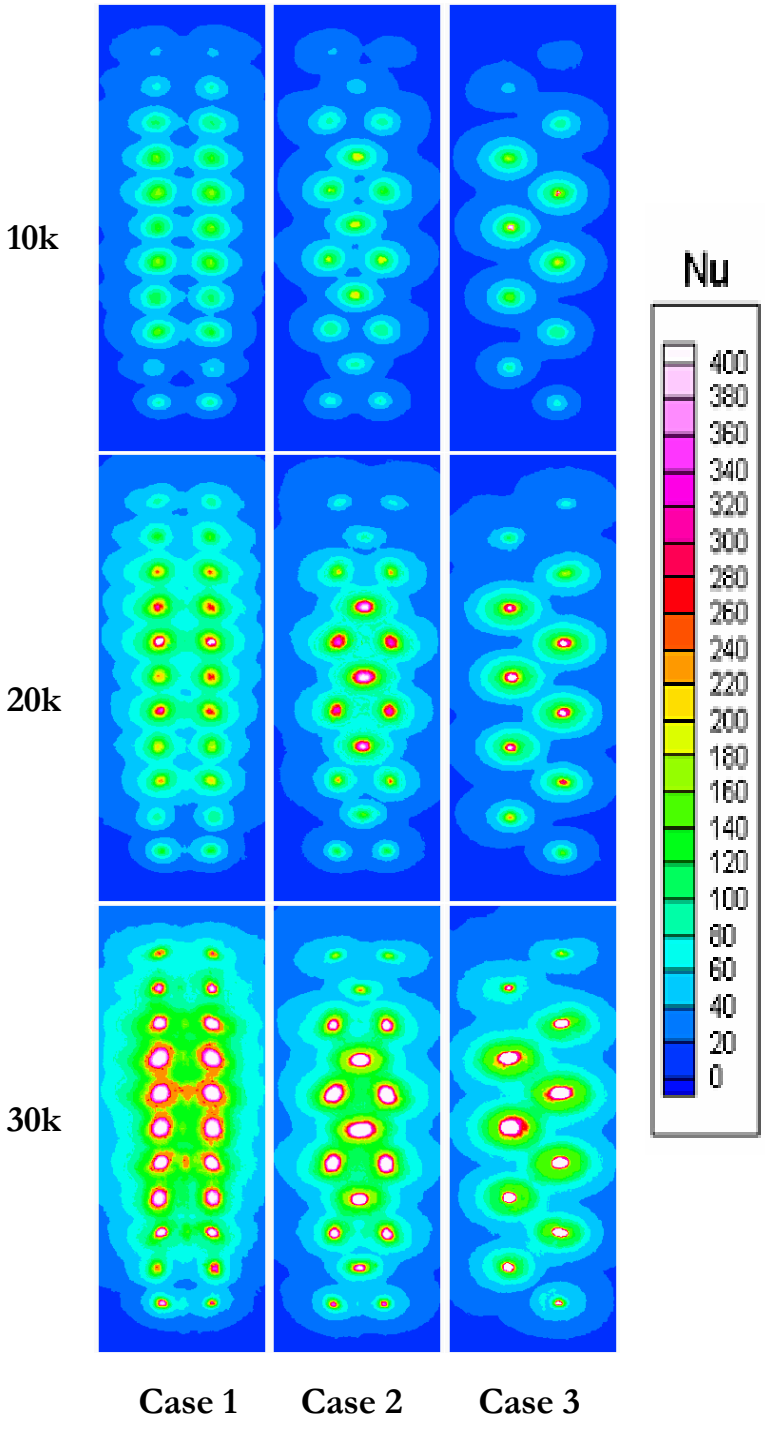

Figure 42: Detailed Nu_D Distributions for Part II

In Case 2, stretching of the jet contact area in the spanwise direction was more evident, especially for the jets located at the center of the jet plate. Due to the staggered nature of the jet pattern, some jet-to-jet interaction was seen in this configuration. However, the interactions had no detrimental effects on the heat transfer characteristics of the impingement array. In Case 3, the sparse, staggered nature of the impingement array produced little to no jet-to-jet interactions with every other impingement jet exiting to opposite sides of the impingement channel. The regions between jets in this configuration showed low Nu_D distributions due to lack of overall coverage, but clear, pure impingement did appear to exist at each jet location.

It should be noted that a decline in heat transfer coefficients was seen in the outer most jet rows in all test cases. Crossflow interactions were not believed to be the principal cause of this reduction. Rather, non-uniform jet velocities due to pressure variations in the inlet section seem to be the main reason why lower Nu_D were obtained at the outer locations. This effect would be much less apparent in large arrays with a more uniform inlet pressure.

5.2.1 Case 1

Figure 43 shows the spanwise averaged Nu_D distributions for Case 1. In every spanwise averaged Nu_D plot of Part II, Nu_D are averaged in the center third of the test plate. As expected, these spanwise averaged Nu_D also showed a significant reduction in the effects of crossflow on downstream heat transfer. The ideal impingement behavior discussed in Section 1.2 was realized throughout most of the test plate for all Re_D's in Case 1. This ideal, or pure, impingement was characterized by a local maximum Nu_D at the stagnation point directly underneath the jet and a local minimum between the jets. This behavior was also present in Part I but only in the first few upstream impingement jets. The final indication that substantially more effective impingement was being achieved in the zero-crossflow design was that the crossflow induced jet deflection previously discussed is only .89 hole diameters for all Re_D of Case 1. This displacement reached an optimal value of 1.25D in Part I.

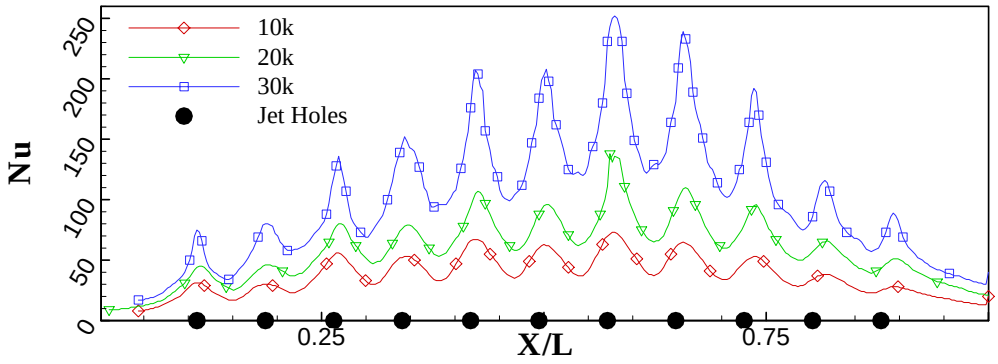

Figure 43: Spanwise Averaged Nu_D for Case 1

5.2.2 Case 2

Figure 44 presents the spanwise averaged Nu_D distributions for Case 2. In this configuration, a single impingement jet located at the center of the plate replaced every other jet row. The total number of impingement jets in this configuration was lowered from 66 to 51, thus the total coolant flow rate was decreased by a factor of 1.3. The reduction of impingement jets at the second, fourth, sixth, eighth, and tenth jet rows produced lower Nu_D peaks due to the existence of only one impingement jet at these locations. In this case, peak Nu_D displacements also reached a maximum of .89 holes diameters. Finally, the symmetric heat transfer pattern seen in Case 1 was also realized in the spanwise average Nu_D plots of Figure 44 showing that heat transfer in these impingement configurations were indeed independent of the exit flow direction.

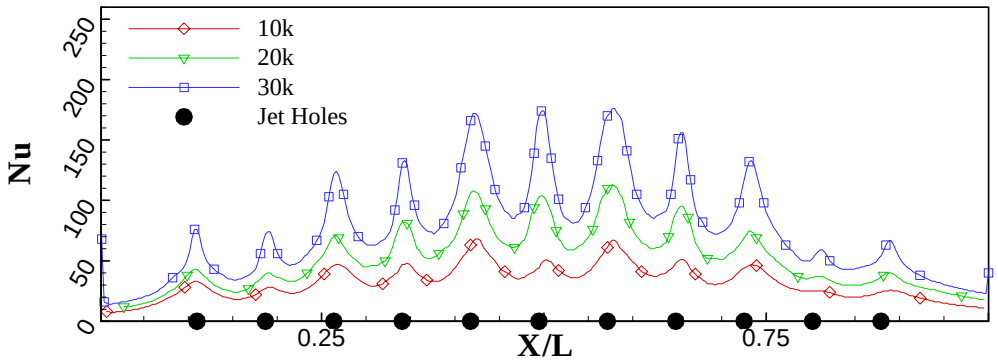

Figure 44: Spanwise Averaged Nu_D for Case 2

5.2.3 Case 3

Figure 45 presents the spanwise averaged Nu_D distributions for Case 3. Recall in the Case 3 there was only one impingement jet at every jet row location. These impingement jets were aligned in a staggered manner. This led to only 33 impingement jets, which used half the total coolant flow rate of Case 1. Much lower Nu_D were seen between the jets in this configuration, mainly due to the large reduction in jet-to-jet interactions. Little to no peak heat transfer occurred at the outermost jet rows. Again, this was not a result of crossflow interactions. Reduced heat transfer was seen because of low jet velocities in those outer regions. Despite a lower magnitude of heat transfer, Case 3 exhibited the same symmetric, zero-crossflow patterns displayed in the previous cases. Again, very little jet contact deflection was seen, and a maximum jet deflection of .89D was reached at the last jet row.

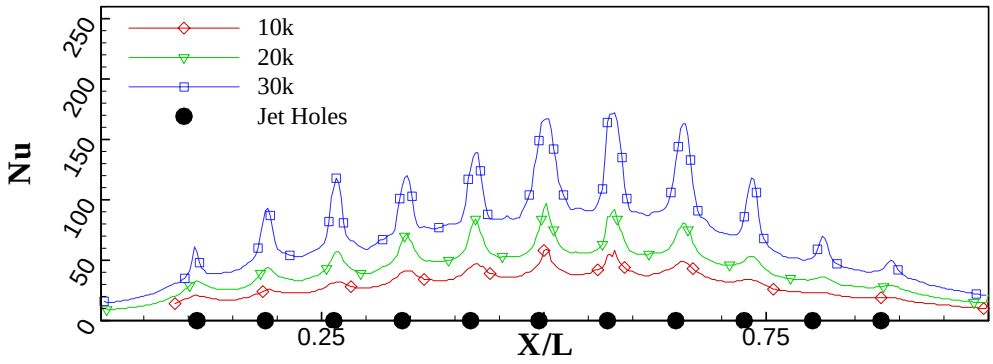

Figure 45: Spanwise Averaged Nu_D for Case 3

5.2.4 Area Average Nusselt Numbers

Figure 46 presents the area averaged Nusselt numbers computed for all cases in Part II. This data was obtained by taking the average of the Nu_D over the area in the central third of the test plate. Generally, a linear relationship between Re_D and area averaged Nu_D is seen on a log-log plot of these quantities. This behavior was seen in Part I of this study. However, in Part II a clear increase in heat transfer is seen at Re_D=30k for all test cases. The result may be attributed to

reduced crossflow interactions, which generally dominate higher Re_D impingement tests. The validity of this conclusion needs to be confirmed through experiments at more jet Re_D's. Similar to Part I, larger coolant flow rates produced larger area averaged Nu_D's, however this behavior was not linearly proportional to coolant mass flow rate. The sparse jet array of Case 3, which has 50% of the coolant flow of Case 1, showed almost 70% of the heat transfer capacity of Case 1. This result along with similar conclusions from Part I of this study and Gao et al [31] suggest that sparse impingement jet arrays may be a more efficient method of heat transfer.

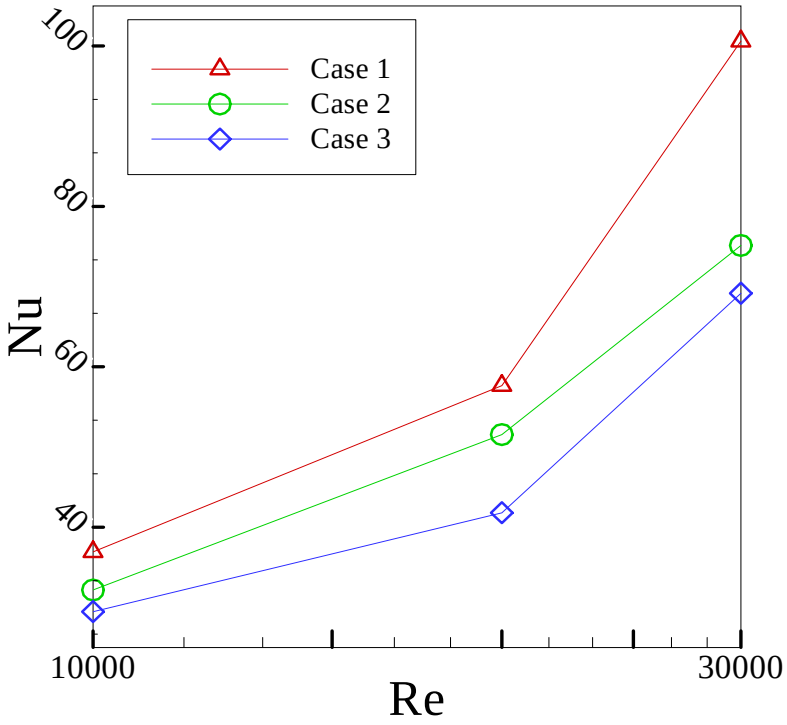

Figure 46: Part II Area Averaged Nu_D

CHAPTER 6

CONCLUSIONS

In this study, two different methods of improving impingement cooling for gas turbine combustors were examined. Part I examined a combination of trip strips and sparse impingement arrays, and Part II examined a zero-crossflow impingement design. Detailed heat transfer distributions were presented for each of these configurations. In Part I, results showed that the placement of ribs enhances downstream heat transfer through more effective impingement. Ribs between the jets produces less crossflow induced degradation and thus higher impingement heat transfer. The overall effect was to reduce the impingement through flow and provide similar levels of heat transfer at the same jet Reynolds number as pure impingement. Alternating ribs with impingement produced the best overall performance with respect to reduced coolant flow requirements and heat transfer level. This was the first study to investigate the combination of impingement with respect to trip strip locations on a test surfaces.

While the trips strips in Part I showed an ability to increase heat transfer, they were not able to completely eliminate crossflow degradation. The innovative impingement channels studied in Part II succeeded in this regard. Detailed Nu_D distributions for all cases showed an overwhelming independence to the direction of the exit flow. This fact was displayed in several ways, such as the lack of jet stretching and fairly uniform heat transfer across the test plate. The most significant indication of these substantial crossflow reductions was the production of symmetric heat transfer distributions with respect to a spanwise axis at the center of the jet plate. Overall, a promising design for maximizing the benefits of jet impingement heat transfer has been proposed with results showing success.

REFERENCES

[1] Lefebvre, Arthur H. Gas Turbine Combustion. Ann Arbor: Taylor & Francis, 1999.

[2] Incropera, Frank P., and David P. DeWitt Introduction to Heat Transfer. 3rd ed. New York: John Wiley & Sons, 1996.

[3] Chupp, R. E., H. E. Helms, P. W. McFadden, and T. R. Brown "Evaluation of Internal Heat Transfer Coefficients for Impingement Cooled Turbine Blades." AIAA Journal of Aircraft Vol. 6, 1969: pp. 203-208.

[4] Kercher, D. M. and W. Tabakoff "Heat Transfer by a Square Array of Round Air Jets Impinging Perpendicular to a Flat Surface Including the Effect of Spent Air." ASME Journal of Engineering and Power Vol. 92, 1970: 73-82.

[5] Chance, J. L. "Experimental Investigation of Air Impingement Heat Transfer Under an Array of Round Jets." TAPPI Vol. 57, 1974: 108-112.

[6] Florschuetz, L. W., R. A. Berry, and D. E. Metzger "Periodic Streamwise Variation of Heat Transfer Coefficients for Inline and Staggered Arrays of Circular Jets with Crossflow of Spent Air." ASME Journal of Heat Transfer Vol. 102, 1980: 132-137.

[7] Florschuetz, L. W., C. R. Truman, and D. E. Metzger "Streamwise Flow and Heat Transfer Distribution for Jet Impingement with Crossflow." ASME Journal of Heat Transfer Vol. 103, 1981: 337-342.

[8] Behbahani, A. I. and R. J. Goldstein "Local Heat Transfer to Staggered Arrays of Impinging Circular Air Jets." ASME Journal of Engineering and Power Vol. 105, 1983: 354-360.

[9] Florschuetz, L. W., D. E. Metzger, and C. C. Su "Heat Transfer Characteristics for Jet Array Impingement with Initial Crossflow." ASME Journal of Heat Transfer Vol. 106, 1984: 34-41.

[10] Downs, S.J. and E. H. James "Jet Impingement Heat Transfer - A Literature Survey." ASME Paper No. 87-HT-35, 1987.

[11] Huber, A.M. and R. Viskanta "Comparison of Convective Heat Transfer to Perimeter and Center Jet in a Confined, Impinging Array of Axisymmetric Air Jets." International Journal of Heat and Mass Transfer Vol. 37, 1994: 3025-3030.

[12] Huber, A.M. and R. Viskanta "Effect of Jet-Jet Spacing on Convective Heat Transfer to Confined, Impinging Arrays of Axisymmetric Air Jets." International Journal of Heat and Mass Transfer Vol. 37, 1994: 2859-2869.

[13] Van Treuren, K.W., Z. Wang, P. T. Ireland, and T. V. Jones "Detailed Measurements of Local Heat Transfer Coefficient and Adiabatic Wall Temperature Beneath an Array of Impingement Jets." ASME Journal of Turbomachinery Vol. 116, 1994: 369-374.

[14] Huang, Y., S. V. Ekkad, and J. C. Han "Local Heat Transfer Coefficient Distribution Under an Array of Impinging Jets Using a Transient Liquid Crystal Technique." AIAA Journal of Thermodynamics & Heat Transfer Vol. 12, 1998: 73-79.

[15] Bailey, J. C. and R. S. Bunker "Local Heat Transfer and Flow Distributions for Impinging Jet Arrays of Dense and Sparse Extent." ASME Paper GT-2002-30473, 2002.

[16] Ekkad, S. V., L. Gao, and R. T. Hebert "Effect of Jet-to-Jet Spacing in Impingement Arrays on Heat Transfer," ASME Paper IMECE2002-32108, New Orleans, La, 2002.

[17] White, D. J., A. Batakis, R. T. Le Cren, and H. G. Yacabucci "Low NOx Combustion Systems for Burning Heavy Residual Fuels and High Fuel-Bound Nitrogen Fuels." Journal of Engineering for Turbines and Power Vol. 104, 1982: 377-385.

[18] Roberts, P. B., A. J. Kubasco, and N. J. Sekas "Development of a Low NOx Lean Premixed Annular Combustor." Journal of Engineering for Turbines and Power Vol. 104, 1982: 28-35.

[19] Smith, K. O., L. C. Angello, and F. R. Kurzynske "Design and Testing of an Ultra-Low NOx Gas Turbine Combustor." ASME Paper 86-GT-263, 1986.

[20] Smith, K. O., A. C. Holsapple, H. H. Mak, and L. Watkins "Development of a Natural Gas-Fired, Ultra-Low NOx Can Combustor for a 800kW Gas Turbine." ASME Paper 91-GT-303, 1991.

[21] Smith, K. O. and L. H. Cowell "Experimental Evaluation of a Liquid Fuels, Lean Premixed Gas Turbine Combustor." ASME Paper 89-GT-264, 1989.

[22] C. J. Etheridge "Mars SoLONOx Lean Premix Combustion technology in Production." ASME Paper 94-GT-255, 1994.

[23] Chin, J., S. Skirvin, L. Hayes, and F. Burggraf "Film Cooling with Multiple Slots and Louvers – Part 1: Multiple Continuous Slots." Journal of Heat Transfer Vol. 83, 1961: 281-286.

[24] Schulz, A "Combustor Liner Cooling Technology in Scope of Reduced Pollutant Formation and Rising Thermal Efficiencies." Heat Transfer in Gas Turbine Systems: Annals of the New York Academy of Sciences Vol. 934, 2001: 135-146.

[25] Han, J. C., L. R. Glicksman, and W. M. Rohsenow "An Investigation of Heat Transfer and Friction for Rib-Roughened Surfaces," International Journal of Heat and Mass Transfer Vol. 21, 1978: 1143-1156.

[26] Han, J. C. "Heat Transfer and Friction in Channels with Two Opposite Rib Roughened Walls," ASME Journal of Heat Transfer Vol. 106, 1984: 774-781.

[27] Han, J. C. "Heat Transfer and Friction Characteristics in Rectangular Channels with Rib Turbulators," ASME Journal of Heat Transfer Vol. 110, 1988: 321-328.

[28] Han, J. C., J. S. Park, and C. K. Lei "Augmented Heat Transfer in Rectangular Channels of Narrow Aspect Ratios with Rib Turbulators," International Journal of Heat and Mass Transfer Vol. 32, 1989: 1619-1630.

[29] Ekkad, S. V. and D. M. Kontrovitz "Jet Impingement Heat Transfer on Dimpled Target Surfaces," International Journal of Heat and Fluid Flow Vol. 23, 2002: 22-28.

[30] Bailey, J. C., J. Intile, T. F. Fric, A. K. Tolpadi, N. V. Nimalan, and R. S. Bunker "Experimental and Numerical Study of Heat Transfer in a Gas Turbine Combustor Liner," ASME Paper GT2002-30183, 2003.

[31] Gao, L., S. V. Ekkad, and R. S. Bunker "Heat Transfer Under Stretched Arrays of Impinging Jets," ASME IGTI Paper GT-2003-38178, 2003.

[32] Hebert, R. T., L. Gao, S. V. Ekkad, and R. S. Bunker "Effect of Streamwise Pressure Gradient on Jet Impingement Heat Transfer," 6th ASME ISHMT Joint Conference, India, Jan. 2004.

VITA

Ryan Thomas Hebert is a native Louisianan and was born on August 18, 1979. He received his high school diploma from Catholic High School in New Iberia, Louisiana, in May of 1997. Next, he attended Louisiana State University where he obtained the degreee of Bachelor of Science in Mechanical Engineering in December of 2002. Ryan then entered the Louisiana State University Graduate School to pursue further education. As of May 2004, he has completed all the requirements to obtain the degree of Master of Science in Mechanical Engineering, which he will officially receive in August of 2004. Ryan has obtained employment with Florida Turbine Technologies in West Palm Beach, Florida, where he will work as a gas turbine durability engineer.